Additive Manufacturing 115 (2026) 105055

Contents lists available at ScienceDirect

Additive Manufacturing

journal homepage: www.elsevier.com/locate/addma

Research paper

Multimodal synchrotron characterization of the formation and spatial distribution of retained austenite in PBF-LB/M-manufactured ferritic–martensitic steel

Natan Garrivier [a,*], Steven Van Petegem [b], Manuel Pouchon [a], Markus Strobl [c], Enrico Tosoratti [d], Adam Cretton [e], Ken Vidar Falch [f], Dario Ferreira Sanchez [g], Malgorzata Grazyna Makowska [a,g]

[a] Advanced Nuclear Materials Group, PSI Center for Nuclear Engineering and Sciences, Paul Scherrer Institute, Forschungsstrasse 111, 5232 Villigen, Switzerland
[b] Structure and Mechanics of Advanced Materials, PSI Center for Photon Science, Paul Scherrer Institute, Forschungsstrasse 111, 5232 Villigen, Switzerland
[c] Laboratory for Neutron Scattering and Imaging, PSI Center for Neutron and Muon Sciences, Paul Scherrer Institute, Forschungsstrasse 111, 5232 Villigen, Switzerland
[d] Innovation Center for Additive Manufacturing, Fürstenlandstrasse 122, 9014 St., Gallen, Switzerland
[e] Department of Physics, Technical University of Denmark DTU, Fysikvej Building 307, 2800 Kgs. Lyngby, Denmark
[f] Hard X-ray Micro/Nano-Probe Beamline, Deutsches Elektronen-Synchrotron DESY, Notkestr. 85, 22607 Hamburg, Germany
[g] Laboratory for Synchrotron Radiation and Femtochemistry, Paul Scherrer Institute, Forschungsstrasse 111, 5232 Villigen, Switzerland

ARTICLE INFO

Keywords:
Metal additive manufacturing
Martensitic steel
Residual austenite
Synchrotron micro-X-ray diffraction and fluorescence
3D chemical imaging

ABSTRACT

Metal additive manufacturing is a promising route for producing complex, highly customized embedded structures for nuclear fusion environments, such as breeding blankets and divertors. These applications require steels with high thermomechanical stability and resistance to irradiation, yet AM processing often leads to undesired microstructural heterogeneities, including the formation of metastable phases. In this work, we investigate the formation and spatial distribution of retained austenite in Laser Powder Bed Fusion (PBF-LB/M) — processed ferritic–martensitic stainless steel (AISI 415) using multimodal synchrotron-based characterization. Micron-resolution 2D and 3D synchrotron X-ray Diffraction and X-ray Fluorescence mapping, combined with operando XRD during PBF-LB/M, reveal the presence of retained γ-phase in periodic mesostructures at concentrations up to 0.5 wt%, depending on scanning strategy. We demonstrated that this result, gained from volumetric measurements based on μXRD scanning imaging, cannot be gathered by any surface-sensitive technique (*e.g.* EBSD) due to depth limitations and phase transformation artifacts during sample preparation. No correlation between γ-phase formation and elemental segregation was observed. Operando XRD measurements show that cooling rates critically affect phase evolution: wall-like geometries exhibit rapid cooling ($\sim 10^5$ to 10^6 K/s) and complete martensitic transformation, whereas bulk samples cool more slowly ($\sim 10^4$ K/s), allowing up to 0.5 wt.% of γ-phase to be retained. These results demonstrate the strong influence of both scanning strategy and thermal history on phase stability in PBF-LB/M steels, supporting the qualification of AM-built components for nuclear applications.

1. Introduction

Advances in nuclear fusion reactors core architecture have led to the consideration of metallic additive manufacturing (AM) as one of the prime manufacturing processes, especially for components with highly complex internal structures such as the breeding blanket and divertor with internal network of cooling/breeding channels and sensors inlets [1]. Therefore, metallic AM techniques like Laser Powder Bed Fusion (PBF-LB/M, shortened to PBF in this article) and Laser Directed Energy Deposition (DED) appear to be a very attractive — if not the only viable solution to produce such elements, considering the volume of production, the dimensions and spatial accuracy requirements of the parts, sometimes in the 100-microns range [2,3]. Several classes of materials that exhibit promising adequate thermo-mechanical and radiation-ageing properties as structural materials are being developed — *e.g.* Vanadium alloys [4,5], SiC/SiC composites [6], Zirconium alloys [7], oxide dispersion-strengthened (ODS) steels [8,9].

* Corresponding author.
E-mail address: natan.garrivier@psi.ch (N. Garrivier).

https://doi.org/10.1016/j.addma.2025.105055
Received 12 August 2025; Received in revised form 11 November 2025; Accepted 15 December 2025
Available online 24 December 2025

Nevertheless, the baseline and primary candidate for structural components of fusion reactors (such as blankets and test blanket modules) remains reduced activation ferritic–martensitic steels (RAFM), due to their radiation resistance resulting in low swelling, thermal stability, low activation, and cost-effectiveness [8–11]. However, because of the characteristic extreme temperature cycling, heating and cooling rates caused by rapid laser melting and solidification during PBF and DED, the properties of alloys produced with AM can strongly differ from those produced by conventional methods [12,13]. For both PBF and DED, the melting of metal powder material is typically done by scanning line-by-line with a defined hatch distance and layer thickness. The final properties of the densified material are determined by the rapid solidification occurring after laser exposure, but are also affected by the consecutive scan lines processed before and after each one, as well as by the layers printed above. This volume of heat-affected material is commonly designated as the Heat-Affected Zone (HAZ). By inducing thermal cycling over the whole printing process, the micro-structure is affected throughout by recrystallization, precipitation, formation of new phases and chemical segregation [14,15]. There are several consequential phenomena to be minded in the scope of nuclear applications. Firstly, the possible formation of minor phases such as retained or reformed austenite grains, carbides, and oxides, all potentially affecting mechanical properties, corrosion and irradiation resistance. Then, grain boundary precipitates, such as Cr_xC_y or Fe–Cr intermetallic σ-phase with the potential to affect radiation resistance and corrosion behavior (certain phases acting as sites for void formation under radiation exposure). Lastly, internal residual stresses in as-built components or columnar/anisotropic grain structures [14,16,17].Typically, RAFM steel would be exposed to a process of recrystallization that could remove the retained austenite, however, retained austenite can have an impact on microstructure in steels and in particular on formation of reversed austenite during pos-manufacturing heat treatment [13,18].

The interplay of rapid cyclic reheating and non-equilibrium solidification, inherent to laser-based AM processes, often results in spatially heterogeneous phase distributions of minor crystalline phases, including retained or reverted austenite (γ-phase). The formation of reverted austenite was predicted to be linked to C atoms segregation in [19], yet this was not directly confirmed experimentally. These conclusions were based on Atom Probe Tomography analysis, which did not allow for quantification of the size and volume fraction of retained austenite. The γ-phase is typically undesirable in RAFM steels due to its reduced high-temperature stability and potential to degrade mechanical performance under neutron irradiation [16,20]. The volume fraction and stability of reverted austenite depends on aging temperature and subsequent cooling rates, with higher temperatures resulting in more reverted austenite but lower stability [21].

Retained austenite in PBF-processed martensitic maraging steels typically arises from factors spanning the solidification process and subsequent heat treatments. Chadha et al. report that rapid cooling (approx. 10^6 K/s) during solidification of a 18Ni-9Co-5Mo PBF maraging steel yields approximately 5% retained austenite forming during solidification after laser processing [22], while Lyu et al. demonstrated that energy input during PBF influences the retained austenite amount, with low input yielding a microstructure with little retained austenite [23]. Given that austenite crystallites form at [24] or right below [19] melt pool boundary, the influence of melt pool characteristics on microstructure evolution stands out as an important factor to understand the process of retained and reformed austenite formation.

Recent operando XRD studies performed during PBF of maraging steel allowed tracking of real-time phase kinetics, showing that rapid heating (500 K/s) and tempering in the 610–650 °C range produce austenite with high thermal stability (*i.e.* retained after cooling) due to localized Ni segregation, while tempering at 690 °C causes near-complete homogenization, leading to unstable austenite that reverted to martensite upon cooling. The technique captures dynamic phase fractions and links thermal stability to elemental partitioning during tempering [25]. Regions with > 5 vol% γ-phase typically exhibit hardness reductions of nearly 25% compared to fully martensitic zones, attributable to austenite's lower intrinsic strength and its role in disrupting martensitic lath continuity [26].

Recrystallization of the main steel phase and precipitation of new phases may be a limiting factor for nuclear applications where materials with a fine grain structure, isotropic properties and high thermomechanical reliability are required [8]. The dynamic processes driving those transformations are yet to be understood, although a relatively large amount of work has been conducted on simulating those mechanisms [27–32]. Parametric studies based on ex-situ investigations, such as X-ray Diffraction (XRD), Fluorescence (XRF), optical and electron microscopy, X-ray and neutron tomography as well as tomographic microscopy, plus neutron diffraction [33–35], provided some knowledge about the material after AM, but cannot address the process dynamics. Operando XRD experiments allow tracking the formation of crystallographic phases, local temperature and heating/cooling rates during laser metallic AM with temporal resolutions down to 25 μs [36]. Operando imaging can provide direct insight into melt pool dynamics and defect formation [37–39]. The outcome of such operando studies can be directly used for validation of numerical models that aim to simulate laser AM processes [40–42].

In order to most accurately describe highly multidimensional processes such as laser AM, a multimodal characterization approach is essential to detect and map unexpected defects and microstructures that may arise in the bulk of laser AM samples, both in 2D and in 3D. The combination of characterization techniques provides thorough insights into the spatial distribution, morphology, and crystallographic characteristics of these features and their implications on macroscale properties [43–45].

This work presents the results of multimodal characterization studies on PBF-manufactured, soft Ferritic–Martensitic (FM) steel samples, which reveal the formation of localized metastable austenite structures. 2D and 3D synchrotron μXRD and μXRF scanning imaging is a technique with great potential for studies dedicated to observe and later tailor specific minor phases in various metallurgical systems. This study employs this technique to systematically detect, map, and analyze the formation of domains containing metastable austenite within AM FM steel, and to link it to the local chemical composition [46–49]. Operando XRD is then used to capture transient phase evolution during laser melting and solidification.

The main objective of this work is to investigate the effects of scanning strategy and cooling rates on the resulting microstructure during PBF of FM steel. Doing so operando (*i.e.* during the process) is of special relevance, as understanding transient phenomena – *e.g.* transitory phase dynamics and metastable phases formation – is absolutely crucial to describe and anticipate the final characteristics of the printed material, which can be of critical interest for nuclear applications.

2. Experimental

2.1. Materials

The material used in this work is a prealloyed, gas-atomized spheroidal soft ferritic–martensitic stainless steel (MetcoAdd 415) powder with a chemical composition similar to 1.4313/X3CrNiMo 13–4 (DIN EN 10088/AISI 415/UNS S41500), produced by Oerlikon Metco and sold at a nominal particle size range of [15-45] μm (Table 1). The particle size distribution (PSD) was measured using a Bettersizer S3 Plus laser diffraction device (Dandong Bettersize Instruments Ltd.) and is shown in supplementary material SM.1.

This alloy composition has good corrosion resistance and a better strength and toughness than most martensitic steels, resulting in better performance under high thermomechanical loads, and was thus selected as a strong candidate for tokamak-style blanket component production [50]. All specimens were built by PBF-LB/M (Aconity Midi+

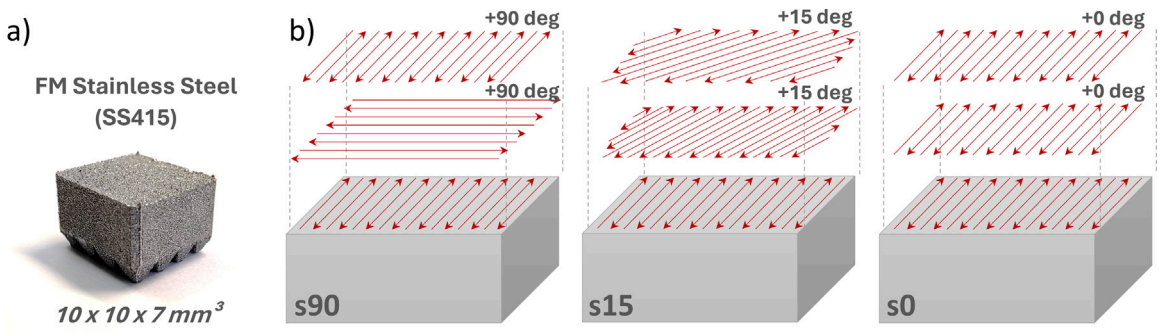

Fig. 1. In this work, one specific sample representative of each batch is presented. (a) Ferritic–Martensitic 415 stainless steel cubes produced by PBF. The standard dimensions of one sample cube are 10 x 10 x 7 mm^3, including the feet structure. (b) Samples printing scanning strategies: **s90:** 90° rotation between layers; **s15:** 15° rotation; **s0:** No rotation.

Table 1
Supplier-certified chemical composition of the powder feedstock.

Weight Percent (nominal)								
	Fe	Cr	Ni	Mo	Mn	Si	C	Rest
MetcoAdd 415	81.8	12.8	3.9	0.5	0.5	0.4	0.017	0.083

with a 400 W Nd:YAG laser) on top of 10 mm thick, 100 mm diameter 316L stainless steel build plates, under < 2000 ppm Nitrogen (N_2) atmospheres. The samples were designed with support stubs, thus minimizing the contact surface area and influence of the buildplate and making removal possible with light hammering. The build plates were wiped with ethanol before the building process.

A parameter study was first conducted to obtain an acceptable ($\gtrsim$ 99.8%) steel bulk density for subsequent microstructure studies. After a preliminary literature review to narrow down the parameters window, a batch of several samples was made with varying energy density. From this batch, the best parameters retained and presented in Table 2 yielded a 99.84% relative density (measured by Archimedes scale method), which was deemed satisfactory enough for this study. Cuboid steel samples were then built under high-purity nitrogen atmosphere with varying processing parameters (see Table 2) and constant dimensions of 10 x 10 x 7 mm^3 (width x length x height along build direction BD) (Fig. 1a). Notably, three different scanning strategies were implemented (Fig. 1b):

- 90°-rotation between layers (s90);
- A 15° rotation between layers (completing a full 360° rotation over the course of 24 layers) (s15);
- Unidirectional scanning strategy with 0° angle rotation between each layer (s0).

The input volumetric energy density remained constant for all the samples presented and is expressed as E_V $[\frac{J}{mm^3}]$:

$$E_V = \frac{\text{Laser power (W)}}{\text{Scan speed (mm s)} \cdot \text{Hatch distance (mm)} \cdot \text{Layer thickness (mm)}}$$

Selected sample cuboids were cut with a diamond wire cutting saw (Well 3242) into 200–400 μm thick slices. These slices were then polished from both sides using silicon carbide grinding paper with the following grit size steps: 46 μm, 22 μm, 10 μm, 5 μm - then further polished using diamond suspension solutions (Buehler MetaDi) of 3 μm, then 1 μm. As-prepared lamellae samples were used for 2D transmission μXRD and μXRF scanning imaging.

Furthermore, three 10 mm high pillars with a cross section of approximately 300 x 300 μm^2 were cut along the build direction throughout the height of the PBF samples s90, s15 and s0 for μXRD and μXRF analysis in tomographic mode (Table 2 s90, s15, s0).

2.2. 2D and 3D synchrotron μXRD and μXRF mapping

μXRD and μXRF microscopy were performed at two different facilities: at the MicroXAS beamline of the Swiss Light Source (SLS), and at the P06 beamline of the Deutsches Elektronen-Synchrotron (DESY).

2.2.1. Chemical imaging at MicroXAS beamline

The experiments were performed using an X-ray photon energy of 17.25 keV corresponding to a wavelength of 0.7187 Å. The X-ray beam was focused using a Kirkpatrick–Baez (KB) mirror system down to a spot size of 1 x 1 μ m^2, and used to perform raster scanning over various regions of interest of different samples. A more detailed description of the experimental procedure can be found in [46].

The X-ray beam signal is acquired using simultaneously four SDD X-ray Fluorescence (XRF) detectors disposed symmetrically around the sample, and a DECTRIS Eiger 4M detector with a pixel size of 75 x 75 μm^2 and a total active area of 162.5 x 155.2 mm^2. XRF spectra were acquired from 4 angles simultaneously and averaged, followed by analysis using PyMCA python toolbox [51]. The XRD detector was placed at a distance of 10 cm behind the sample, covering an angular range of $0 < 2\theta \leq 48°$. The setup geometry was calibrated using a standard LaB_6 (from NIST), allowing to account for precise measurement geometry, in particular sample-detector relative position. Azimuthal integration of the diffraction rings from the X-ray detector was performed using the pyFAI python package [52]. The resulting 2D XRD maps were plotted and analyzed using in-house developed Matlab® routines and the Fiji distribution of imageJ. The images of the FCC phase distribution were obtained by integration of the surface area under all FCC diffraction peaks after subtraction of the background locally defined separately for each peak. Such background was defined using a narrow 2Θ range near the respective peak. Such procedure allowed for removal of possible artifacts caused by instrument background.

The step size of the 2D raster-scanned maps presented in Section 6 was 5 μm horizontally and 10 μm vertically for the large-scale map, and 1 x 1 μm^2 for the detailed views. Rietveld refinement of the diffraction patterns was performed using Bruker Topas (version 7.13) software.

2.2.2. Chemical imaging at P06

The experiments were performed using an X-ray photon energy of 35 keV corresponding to a wavelength of 0.3542 Å. The beam was focused down to a spot size of 880 x 530 nm^2 using Compound Refractive Lenses (CRLs) and used to perform raster scanning over various regions of interest of six different lamellae and pillars.

The X-ray beam signal is acquired using simultaneously one SDD detector for XRF and a Lambda 2M with Ga-As sensor for XRD, with a pixel size of 55 x 55 μm^2 and a total active area of 85 x 85 mm^2. The Lambda detector was placed at a distance of 10 cm behind the sample, covering an angular range of $7 < 2\theta \leq 35°$. The setup was calibrated

Table 2
Laser processing parameters for ex-situ and operando samples. P: laser power, **v:** laser speed, **d:** laser spot diameter, **t:** layer thickness, **h:** hatch spacing, E: energy density. Ex-situ samples were processed under a nitrogen (N_2) atmosphere, while operando samples were processed under argon (Ar).

Sample	Type	P (W)	v (mm/s)	d (mm)	t (μm)	h (μm)	E (J/mm^3)	Strategy
s90	Ex-situ	180	1000	0.08	30	80	75	0°/90° rotation
s15	Ex-situ	180	1000	0.08	30	80	75	15° rotation spiral hatch
s0	Ex-situ	180	1000	0.08	30	80	75	0° unidirectional
sB	Operando	200	500	0.045	30	40	222	0°/90° "snake" hatching
sW	Operando	200	500	0.045	30	N/A	222	Single-track wall (4.5 mm)

using a standard LaB_6. For data analysis and plotting, the same tools were used as mentioned in the previous subsection.

3D μXRD scanning imaging was done in X-ray transmission mode on 300–400 μm thick pillars extracted from the as-manufactured cubic samples. Each specimen was rotated around the build direction (BD) axis while diffraction patterns were collected over a 180° angular range with a 1° angular step resolution. The experimental setup was the same as described in [47] and the data processed as described in [46]. For each pillar, a series of 3–6 tomographic slices were acquired along the BD axis with a step size of 10 μm for sample s90 and 60 μm for sample s15. The tomography data sets were reconstructed with the filtered back projection (FBP) algorithm using homemade python scripts based on the ASTRA Toolbox library [53,54]. The volume rendering and material segmentation of the reconstructed 3D volume allowing the visualization of metallic phase mesostructures was performed in Avizo Thermofischer (version 9.4).

2.3. Electron microscopy characterization

Samples prepared as described in the previous subsection were further polished using argon ion milling (Ar gas, 6 kV, 85° incidence, 10 min, ±180° rocking angle) to ensure high quality surface of the cross-section. The samples were observed using a Thermo Fisher Scientific Quanta 200F Scanning Electron Microscope (SEM) with a Schottky type field emission gun and a constant 20 kV electron beam through various techniques and working distances ranging from 10.0–18.6 mm. Secondary Electrons (SE) imaging allowed highlighting fine surface topological variations and microstructure; Electron Backscattered Diffraction (EBSD, EDAX Hikari detector) was used for microstructural analysis; EBSD data processing and analysis was conducted on the EDAX OIM Analysis™ software.

2.4. Operando PBF-LB/M XRD at microXAS

Operando X-ray diffraction experiments were performed at the microXAS beamline of the Swiss Light Source synchrotron. Measurements were performed at a photon energy of 17.26 keV, which corresponds to 0.7183 Å. The beam was focused down using a Kirkpatrick–Baez (KB) mirror system to a spot size of 30 x 10 μm^2. The PBF processing was carried out with the MiniSLM device, with the X-ray beam hitting the sample at an incident angle of 17° and as described in [55], resulting in an X-ray beam size of roughly 30 μ m diameter projected onto the sample. The diffracted beam was recorded in X-ray reflection mode by an EIGER 1M detector developed by PSI detector group [56] with a pixel size of 75 x 75 μm^2 and a total active area of 77.9 ×77.2 mm^2. The detector was placed at a distance of 6 cm behind the sample, covering an angular range of $20 < 2\theta \leq 55°$. The detector was operated in 8 bit mode at three frames rates of 5, 10 or 20 kHz. The lower energy threshold was set to 8.63 keV. Detector and processing laser triggering were synchronized via hardware connection. Data analysis was performed using the same softwares as for the ex-situ XRD measurements [57]. Measurements of diffraction patterns for cuboid samples in reflection geometry and single-track wall samples in transmission geometry were recorded *operando*. Representative samples are presented in (Table 2 sB, sW). Sample sB is a 2 x 4 mm^2 cuboid measured in X-ray beam reflection mode at 5 and 10 kHz. Sample sW is a 4.5 mm long, ≈ 150 μm thick single-track wall measured in X-ray beam transmission mode at 20 kHz. These samples were chosen for being representative examples of a bigger batch of manufactured and measured samples.

3. Results

3.1. 2D synchrotron μXRD and μXRF imaging

3.1.1. Effect of laser scanning strategy on the distribution of the austenite phase

Accurate identification and mapping of crystalline phases with 2D XRD-contrast scanning imaging using a sub-micron X-ray beam (performed at the microXAS and P06 beamlines) allowed to correlate their distribution in the bulk to different laser scanning scenarios. These measurements have shown that for each case, solely two crystalline phases were produced: the major phase was the BCC structure, and the second minor phase was the FCC structure. The distribution of the FCC phase and its dependence on the laser scanning direction is described in the following sections.

FCC phase distribution for 90° scanning vector rotation (sample s90). Thin lamellae (< 60 μm thickness) extracted from the sample s90, manufactured with a rotation angle of 90° between subsequent layers, were investigated by chemical imaging at microXAS. Large field-of-view (FOV) scans were performed with a relatively large scanning step size, or spatial resolution of 5 μm (horizontally) x 10 μm (vertically) to investigate an area large enough to represent the entire sample. Such scans have revealed the presence of γ-phase (austenitic phase) inside the primarily $\alpha|\alpha'$-phase matrix. The austenite phase crystallites organized into mesostructures that were observed periodically along the full 3 mm height of the sample (Fig. 2a). Fig. 3(a) shows the XRD pattern integrated from a region covering one "lime green" stripe in Fig. 2(a), clearly outlining the presence of the γ-phase, while the XRD pattern obtained from a region covering one "navy blue" stripe (Fig. 3b) shows a nearly γ-phase-free composition. The chemical elements distribution maps obtained from the concomitantly acquired XRF spectra show no spatial variations, indicating that the observed mesostructures do not stem from chemical segregation of the principal alloying elements such as iron, nickel, and chromium (Supplementary Material SM 4).

The γ-phase weight fraction in sample s90 within the BCC matrix was estimated to be 0.2 wt%, as averaged over the whole region (evaluated by Rietveld refinement). However, locally targeted quantification on single γ-phase rich stripes displays mass contents of up to 1 wt%, while in areas designated as "γ-phase free", the FCC-phase was not detectable. It should be noted that the discussed values of quantified phases fractions in the order of 0.2 wt% are close to the error threshold in Rietveld refinement, even when applied to an almost perfect quality data set. Therefore, in this work, we discuss the detection and comparison of observed amounts of the γ-phase in specific locations of the sample volume, rather than the total phase amount. This method allows comparing different regions with high certainty, however global values should be treated as an estimate.

The coarse resolution used for these scans resulted in large FOV maps representative of the whole sample, and showed high regularity

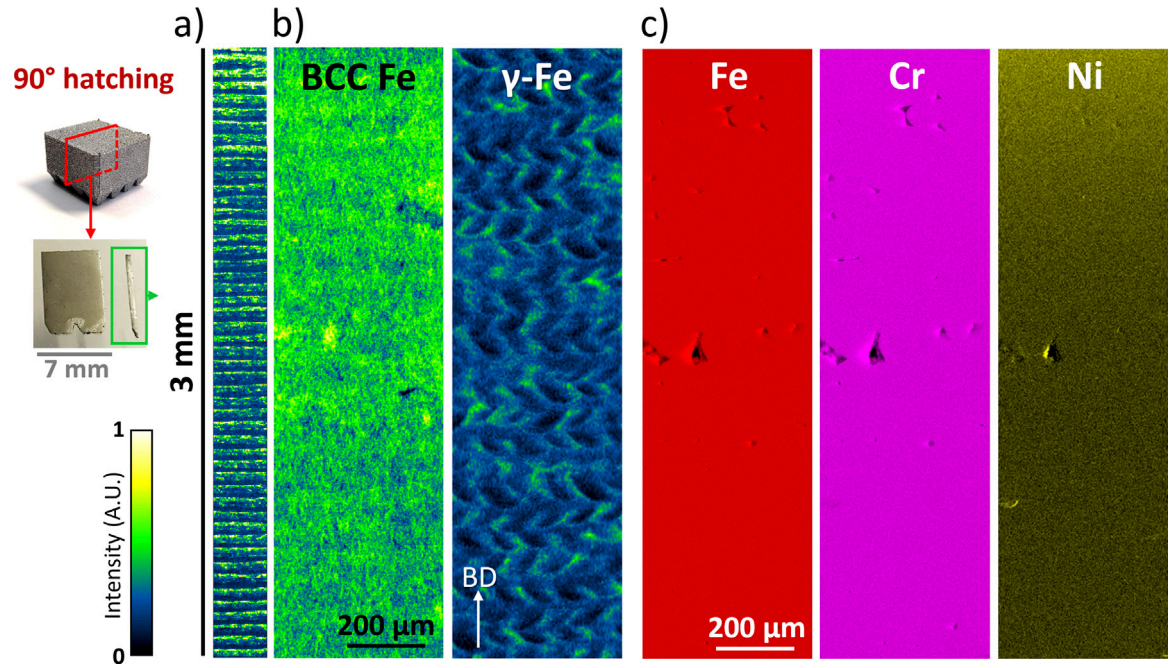

Fig. 2. Pillar sample extracted from a cuboid specimen, as shown on the left-side of the figure. Correlated 2D synchrotron **(a)** transmission XRD mapping performed at microXAS, **(b)** transmission XRD mapping performed at P06, and **(c)** XRF maps of sample s90. Scale bar represents normalized X-ray signal transmission between 0–1. For readability purposes, scale and contrast of each XRF map was optimized to highlight eventual periodical composition structures. Images in **(b)** and **(c)** are obtained for the same ROI.

of the observed structures over the whole probed FOV. The sample thickness (30–40 µm) was smaller than the expected melt pool diameter (80-100μ m — *cf.* Table 2), thus hindering the understanding of the 3D spatial distribution of austenite. To assess the information on the austenitic structures across multiple hatches, measurements using 35 keV X-ray energy – allowing to penetrate thicker samples – were performed at the P06 beamline of the DESY synchrotron. 2D µXRD and µXRF imaging at P06 showed a somewhat similar structure, with an observed pattern periodicity of 120 µm (Fig. 2b). These measurements were performed on a smaller FOV, however with a significantly higher spatial resolution down to 1 x 1 µm^2, which allowed for a better definition of the observed mesostructures. The difference in the perceived morphology of the stripes between Fig. 2(a) and (b) is due to their spatial nature, and is later explained in Section 3.2 by 3D XRD imaging analysis. The ratio of FCC phase- to BCC phase-amount expressed in wt.% is found to reach 0.5 wt% locally, and 0.15 wt% in the whole sample. In this case again, the XRF-contrast images shown in Fig. 2(c) did not reveal any link between chemical segregation of Fe, Cr, Ni and the distribution of retained austenite.

Unidirectional hatching strategy (sample s0). Samples manufactured with a unidirectional, 0° rotation angle between subsequent layers predictably also exhibit a strong anisotropy. XRD-contrast maps revealed a prominent distribution of γ-phase aligning with single-printed tracks. The patterns vary depending on the angle of observation, whether parallel or perpendicular to the printed tracks (respectively, Fig. 4a) and (b), which were made with a resolution of 3 x 3 µm^2. The austenitic phase appears to concentrate around the edge of the melt pool tracks, where the FCC-to-BCC phase weight ratio is the highest, reaching up to 0.5 wt% under a single melt pool track and 0.15 wt% for the entire sample. The γ-phase pattern periodicity is of 30 µm, corresponding to a single printed layer thickness. In the µXRF maps (Fig. 4c), as with all samples present in this work, no segregation of the main alloying elements is visible.

Fig. 5(a) shows the magnified region of the top area of sample s0 presented in Fig. 4, which was mapped at a higher 2D resolution of 1 µm, revealing that the top layers have a significantly lower amount of the γ-phase. This indicates that γ-phase was formed in the lower layers only during deposition of the subsequent layer, by transferring heat to the material below. The dashed lines on the bottom γ-phase map of (b) indicate the borders of each individual laser track. Note how between the two borders, *i.e.* within the meltpool track, amounts of γ-phase (in green) increase from left to right. This supports the argument that retained austenite forms within a track only during subsequent printing of the next one.

15° Scanning vector rotation (sample s15). Samples manufactured with a 15° rotation angle between subsequent 30 µm thick layers exhibit a more complex structure, which is illustrated in Fig. 6, and the pattern repeats every 720 µm along the build direction. The FCC-phase fraction is found to reach 0.5 wt% locally, and 0.2 wt% in the whole sample. Although, the observed pattern showing distribution of FCC phase is clearly periodical, it is not possible to fully understand the complex 3-dimensional distribution of the γ-phase using this 2D images.

3.2. 3D synchrotron µXRD scanning imaging

The results presented in the previous sections have shown that the distribution of γ-phase is directly linked to the laser scanning strategy. However, given the 3-dimensional nature of PBF-built structures, the 2D-imaging results presented in the previous sections may be difficult to interpret, especially for samples manufactured with a 15° rotation of the laser scanning pattern. To fully understand the distribution of the austenitic γ-phase in the sample volume, XRD-contrast imaging was performed in 3 dimensions. Using the same experimental setup as in 3.1.1, samples were scanned slice-by-slice going up the build direction axis using the methodology described in 2.2.2. Two pillars were imaged: sample s15 (15° rotation of scanning pattern) and sample s0 (0° rotation of scanning pattern). Selected tomographic slices acquired for the sample s0 are shown in Fig. 7(a), and several tomographic slices acquired for the sample s15 are shown in Fig. 8(b). More illustrative information about the austenite phase distribution presented in 7(b) is presented in the supplementary video SV1. This video shows a 360°

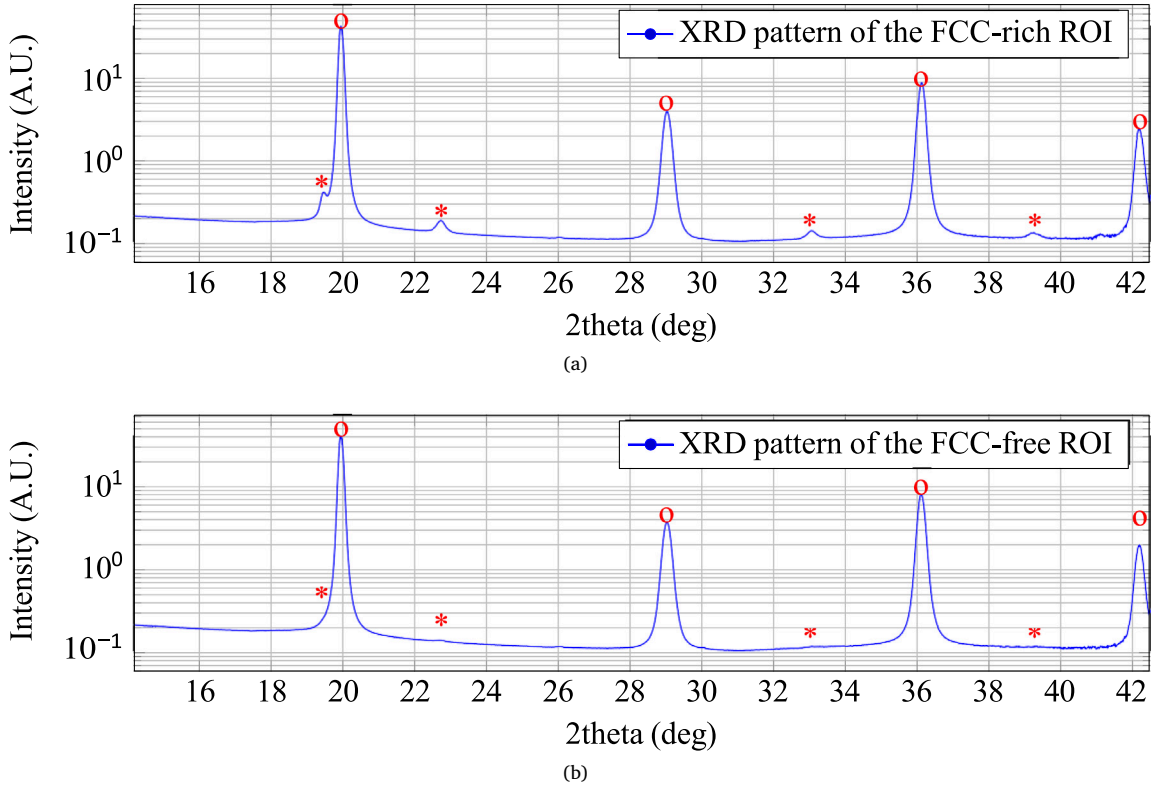

Fig. 3. XRD spectra of the **(a)** γ phase-rich and **(b)** γ phase-free stripes. Markers identify phase-characteristic peaks. [* = γ-phase, o = $\alpha|\alpha'$].

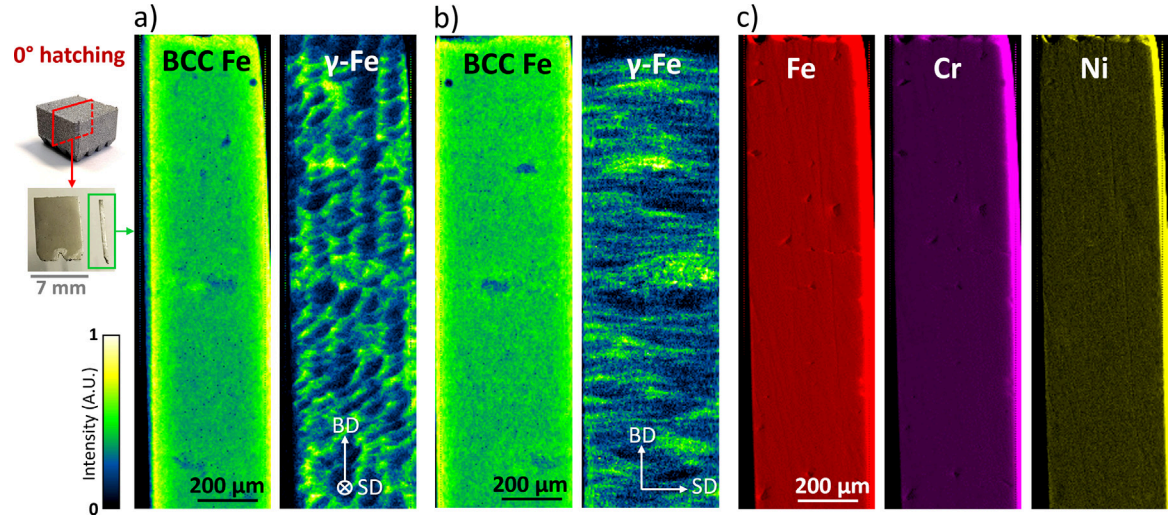

Fig. 4. Pillar sample extracted from a cuboid specimen, as shown on the left-side of the figure. Scale bar represents normalized X-ray signal transmission between 0–1. Crystalline phase mapping probed with the X-ray beam **(a)** parallel and **(b)** perpendicular to the scanning direction (SD), as indicated by white arrows in the image; **(c)** XRF mapping of PBF MetcoAdd 415 steel sample s0. For readability purposes, scale and contrast of each XRF map was optimized to highlight eventual periodical composition structures.

view of the reconstructed γ-phase volume distribution and the raw reconstructed data around a section of a single laser track from s0.

By stitching the consecutive slices from sample s0, it is possible to render the volumetric distribution of the γ-phase in the sample bulk. Results of this reconstruction is shown in Fig. 7(b). The FOV has been adjusted to visualize a volume only slightly larger than the size of a single melt pool track width. The obtained results show the γ-phase rich "walls" forming around the predominantly $\alpha|\alpha'$-phase laser track. The spatial localization of these walls relative to each single printed track is consistent throughout the whole measured volume. These diffuse, γ-phase wall-like structures (Fig. 7c) are precisely what was observed and coined as "stripes" in previously shown 2D maps (Fig. 2a). The periodicity of the structures and their location, bordering the meltpool, indicate that the γ-phase precipitates form alongside the hatching patterns and outside of the solidifying material, in the neighboring heat-affected zone. Fig. 8(a,b) illustrates the reconstructed slices acquired for sample s15, with the corresponding positions on the pillar. The distance between the acquired tomographic slices is equal

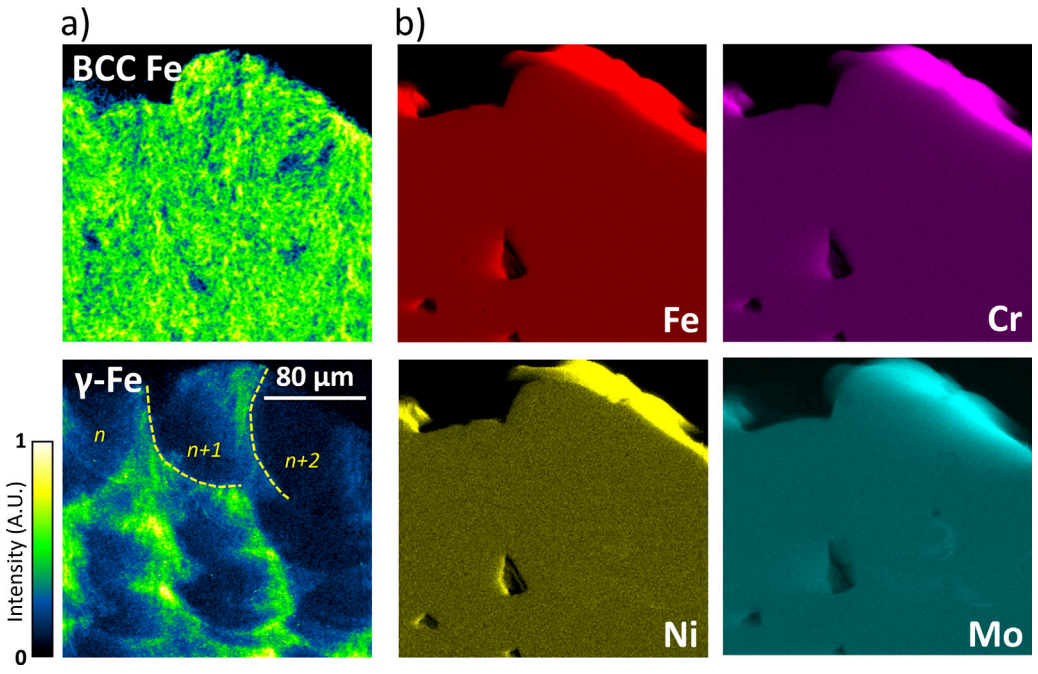

Fig. 5. **(a)** XRD and **(b)** XRF maps of the few last-printed, uppermost layers of the sample with no rotation hatching. The *n, n+1, n+2* numbering indicates the order in which tracks were printed. Scale bar represents normalized X-ray signal transmission between 0–1.

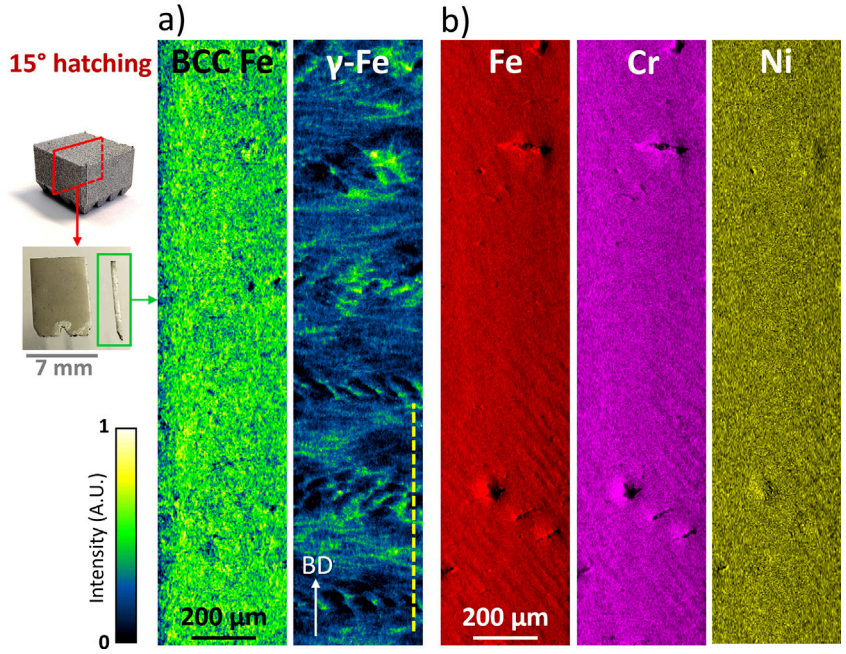

Fig. 6. Pillar sample extracted from a cuboid specimen, as shown on the left-side of the figure. Correlated 2D synchrotron **(a)** transmission XRD and **(b)** XRF mapping of sample s15. The yellow dashed lined indicates the span of one full period of the rotation pattern (720 µm). Scale bar represents normalized X-ray signal transmission between 0–1. For readability purposes, scale and contrast of each XRF map was optimized to highlight eventual periodical composition structures. The visible structures on the bottom half, identical for all three maps, are due to residual surface roughness from sample polishing.

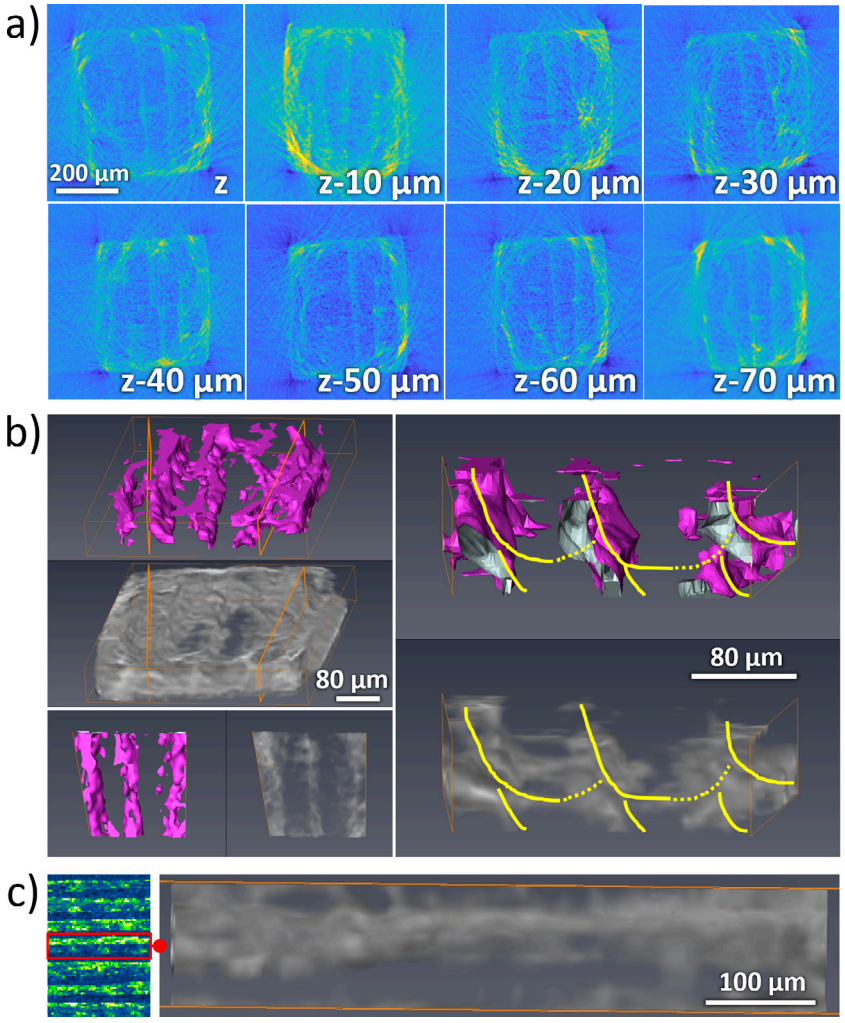

Fig. 7. (a) γ-phase distribution in XRD tomographic slices reconstructed from XRD-contrast scanning imaging of a pillar extracted from sample s0 ; **(b)** 3D reconstructed γ-phase wall-like features surrounding a single portion of laser track ; **(c)** γ-phase distribution pattern. The 2D side view projection of the reconstructed tomographic data from a single printed track correlates with the features shown in Fig. 4.

to 60 µm, which corresponds to 2 layers and to the rotation of the laser scanning pattern by 30°. It should be noted that some slices (2, 3, 4) were apparently acquired close to the center of the layer height, resulting in very clear and regular distribution of the austenite phase, while the other slices (5 and 6) were acquired close to the bottom (or top) of the layers, and therefore exhibit less defined mesostructures.

3.3. Electron microscopy characterization

EBSD mapping shows expected variability in grain morphology, following the characteristic melt pool-shaped nucleation of high-temperature austenitic grains. However, the austenitic mesostructures identified in the images obtained from XRD measured in transmission mode are not visible, even to an expecting eye. Furthermore, a majority of the grains labeled as γ-phase in Fig. 9(b) were identified with a very low confidence index (< 0.1). Crystalline phase maps (Fig. 9b,d) do not allow to discern any larger-scale periodic order. When present, observed grain sizes of γ-phase range from > 100 nm to 1 µm diameter, and are either too far from each other or too small to be accurately mapped with EBSD.

3.4. Operando synchrotron XRD

Figs. 10 and 11 illustrate the results obtained from the operando synchrotron XRD measurements acquired during PBF of sB-type (cuboid) and sW-type (thin wall) samples, respectively.

In the bulky samples (sB-type), the first phase detected after solidification is the high temperature FCC structure (γ-phase). The austenitic phase remains dominant during cooling for about 800 ms, after which the transition to martensite phase starts to take place, indicating that the M_s temperature (start of the austenite-to-martensite transformation) is reached. Nevertheless, Fig. 10(c) shows that the FCC structure remains present until the end of the measurement. Fig. 10(a) shows the significant fraction of austenite in the top layer 3 sec after melting. A surprisingly high amount of retained austenite, amounting to ~ 14 ± 1%, persists through longer cooling periods, as evidenced by the XRD pattern acquired 2–3 min after the process and shown in Fig. 10(c). By this time, the sample has reached a temperature far below any transition temperature for this steel: more specifically M_s, calculated to be 525 °C (798 K) using the equation proposed in [58], and M_f which is expected to be above 400 °C (673 K) as shown in [59]. However, it should be noted that measurements performed at 17.26 keV and 15°

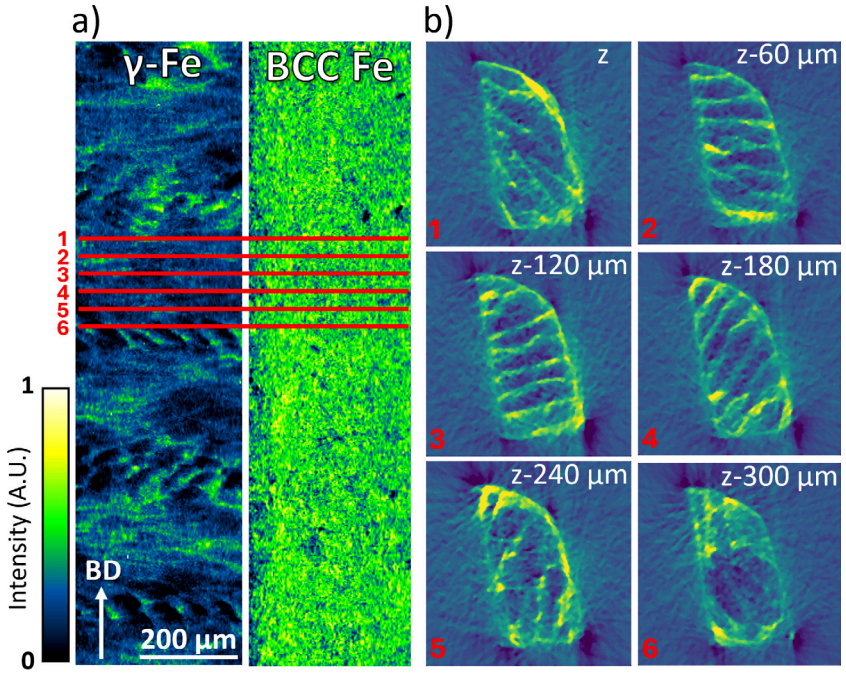

Fig. 8. **(a)** Position of the slices acquired in XRD-contrast scanning imaging of sample s15 pillar; **(b)** γ-phase distribution in XRD tomographic slices reconstructed from XRD-contrast scanning imaging. Scale bar represents normalized X-ray signal transmission between 0–1.

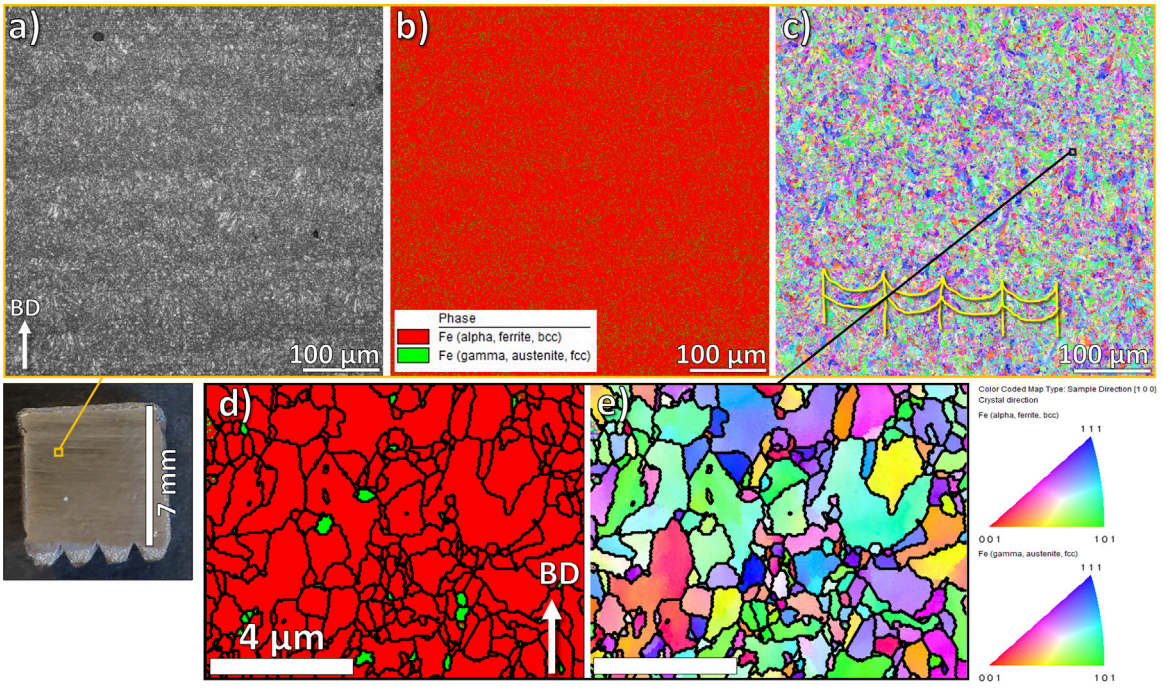

Fig. 9. **(a)** SEM image of a 500 x 500 µm^2 area of the manufactured AISI 415 steel sample, covering 5 periods of the austenitic-rich layers; **(b)** EBSD phase distribution map of the area. Red corresponds to α-phase grains, green to γ-phase grains; **(c)** EBSD Orientation map of the area. Note the fairly visible individual melt pool tracks. **(d)** Detailed EBSD phase map of a 10 x 8 µm^2 area of the manufactured AISI 415 steel bulk, with α-phase in red and γ-phase in green. **(e)** EBSD Orientation map of the area.

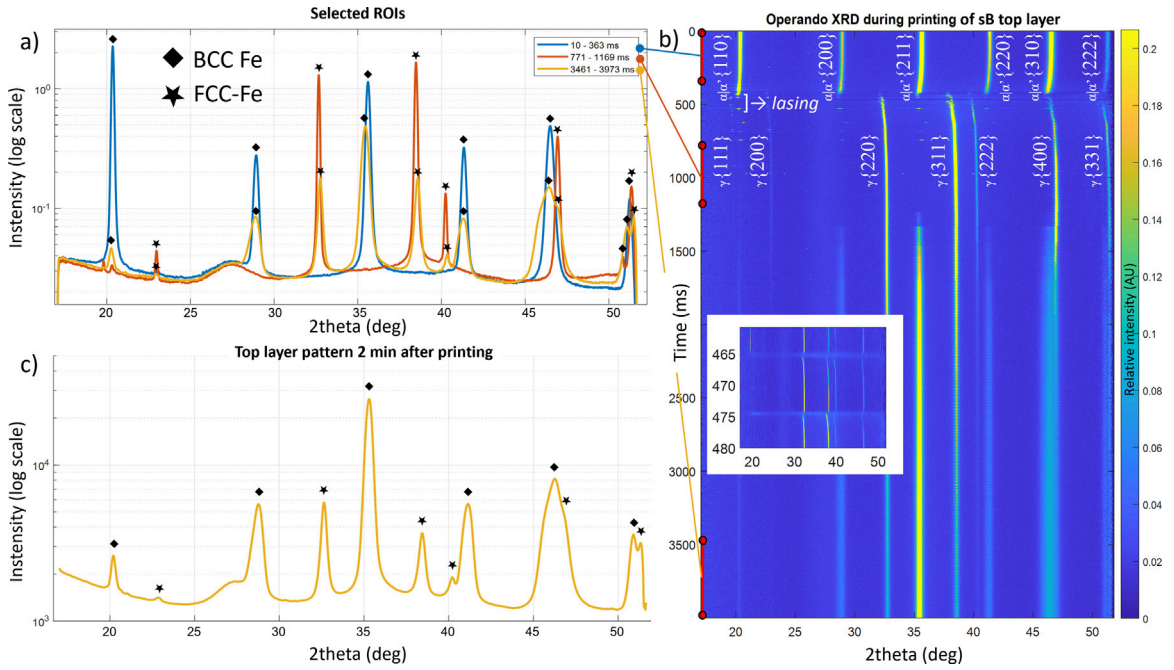

Fig. 10. **(a)** Operando XRD data taken during the printing of cuboid sample sB. Blue curve = powder signal before melting; orange curve = high-temperature, austenitic structure right after lasing; yellow curve = coexisting FCC and BCC iron phases below transition temperature.
(b) Operando XRD signal acquired at 5 kHz during the PBF printing of MetcoAdd 415. The inset shows a zoom in the 460–480 ms period, where a fully molten phase is observed;
(c) Pure 415 steel 2 min after printing layer 3, taken at quasi-room temperature. Diamonds designate $\alpha|\alpha'$-phase peaks, stars designate γ-phase peaks.

incidence angle, illustrated in Fig. 10, only allow to probe a depth of about ≤ 5 µm from the top surface, which does not necessarily reflects the microstructure of the whole layer depth. It should also be noted that γ-phase is not initially detected within the raw deposited powder, as shown in Fig. 10a (blue pattern). Finally, this amount of retained austenite is not to be compared with the results presented in 3.1.1, as these were produced using an entirely different system and set of parameters.

In the case of operando XRD in transmission mode performed on single track walls (*i.e.* sW-type samples), the first phase observed after solidification is the δ-phase (high temperature ferrite) which subsists for only about 1 ms, as highlighted in Fig. 11(c). After 1 ms, the δ-phase disappears and the γ-phase forms, but in contrast to the sB-type samples measurements, it does not subsist more than a couple of hundreds of ms. This is evidenced in Fig. 11a,(b) where the γ-phase characteristic pattern disappears completely $\approx$ 100 ms after lasing, transforming entirely to martensite within 40 ms.

Using the peak position at room temperature as a reference value, and tracking peaks position during cooling, it is possible to infer real-time phase/temperature information [41] and to compute the cooling rates over any period of time. Fig. 12 illustrates the temperature profiles calculated for measurements taken for samples sB and sW, as well as the cooling rates of both samples obtained at the Ae1 and M_s temperature thresholds. M_f is not displayed on this figure, but can be considered to be 100 K below M_s for this alloy composition, *i.e.* $\approx$ 700 K.

The cooling rates observed during printing of wall samples (sW-type) are one order of magnitude higher than during bulk samples (sB-type) manufacturing around the M_s temperature threshold (Fig. 12). This effect is due to the higher heat accumulation during raster scanning *vs.* single-pass mode, and heat loss regimes associated with the two different sample geometries. In bulk samples, we find more than one heat-loss mechanisms; first a fast cooling phase dominated by atmosphere convection and radiation (surface heat loss to atmosphere), then a slow cooling phase dominated by heat conduction inside the material. In the single-wall samples, cooling is largely dominated by radiation heat loss, thanks to an increased surface-to-volume ratio favoring fast cooling rates. As a result, material in the bulky (sB) sample remains above the M_s temperature for a significantly longer time after solidification. This fact, together with a relatively slow cooling rate after reaching M_s, facilitates the retention of the austenite phase.

4. Discussion

4.1. Spatial distribution of the γ-phase

Scanning µXRD mapping (Fig. 2, 4, 5, 6, and 7, 8) outlined the formation of periodical γ-phase mesostructures that follow the shape of meltpool track contours and span homogeneously over the entire volume of the samples. As demonstrated by µXRF imaging in Fig. 2, 4, 5, and 6, the formation of these structures does not stem from segregation of the main alloying elements in the $\alpha|\alpha'$-phase bulk of the sample. On the other hand, the distribution of the austenite phase was observed to be directly linked to the direction of the laser scanning path strategies.

The synchrotron XRD imaging performed in transmission with a sub-micron beam allowed to detect the γ-phase in amounts below 0.01% and to reconstruct its distribution in the bulk in 3 dimensions, without compromising much on spatial resolution. 2D XRD data is gathered through the entire 300–400 µm thickness and integrated along the beam direction. Quantitative analysis of the XRD mapping data shows varying FCC phase fraction, however remaining below 1 wt% in γ-Fe in FCC-rich bands, down to 0 wt% in the FCC-free bands. The 120 µm periodicity of the pattern in sample s90 corresponds to the thickness of 4 powder layers, or when the hatching vector is back to its initial direction. In sample s15, the periodicity is 720 µm and corresponds to 24 layers. In sample s0, it corresponds to the printed layer thickness, *i.e.* 30 µm. Independently from the scanning strategy, measured amounts of γ-phase were coherent with the previously found range of 0 - 1 wt%.

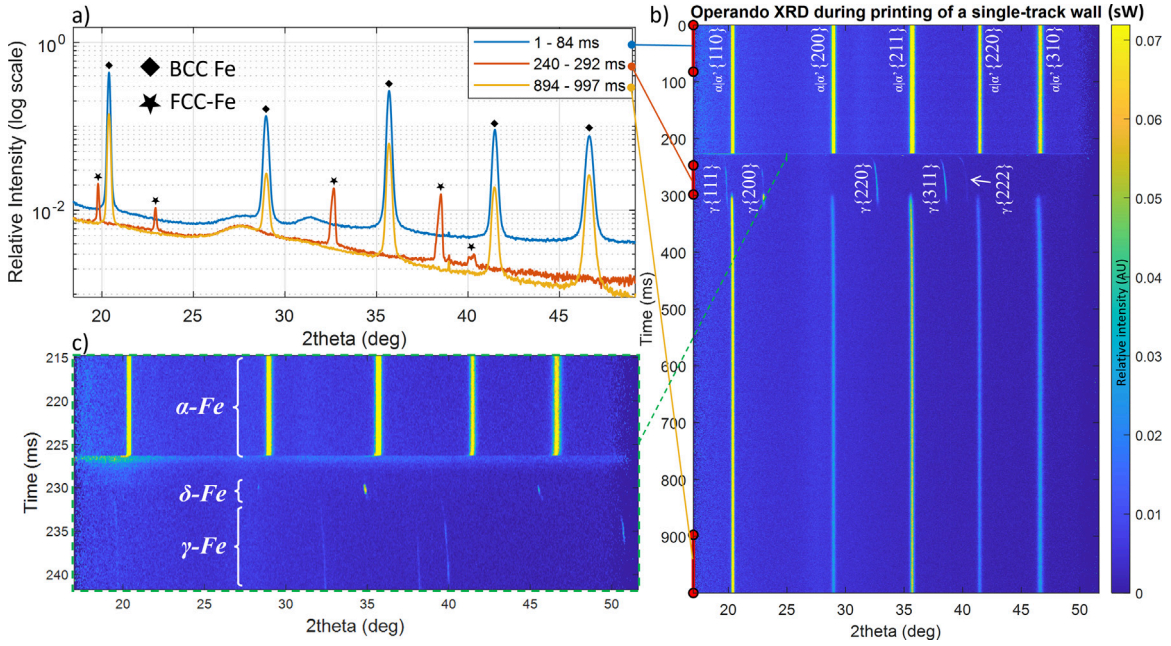

Fig. 11. **(a)** Operando XRD data taken during the printing of single-track wall sample sW. Blue curve = powder signal before melting; orange curve = high-temperature, austenitic structure right after lasing; yellow curve = the material is back to pure BCC phase.
(b) Operando XRD signal acquired at 20 kHz during the PBF printing of MetcoAdd 415;
(c) Signal at the moment of the single laser pass. The acquisition frequency at 20 kHz allows resolving the transitory formation of δ-ferrite during cooling, before transforming to γ.

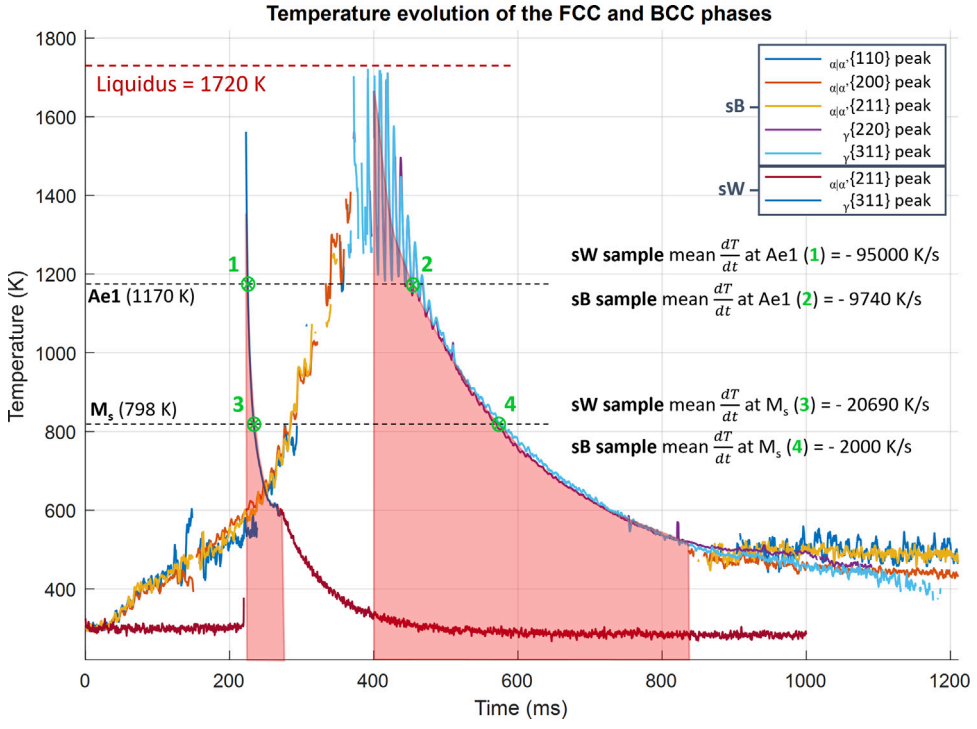

Fig. 12. Comparison of cooling rates of $\alpha|\alpha'$- and γ phases in cuboid bulk and wall samples sB (bulk sample) and sW (wall sample), respectively.

Notably, the amount of austenite phase observed in the top layer (0 to 30 μm down from the surface) was significantly lower than in the layers below, indicating that the retained austenite is not formed during the solidification and cooling of a new layer, but during reheating while the next layer is deposited above.

Conservation of a portion of austenite into retained austenite, as described in [19], is proposed as an origin of the observed austenitic mesostructures observed in this work for 415 stainless steel PBF samples. No segregation of main alloying elements is observed at this scale, as atomic diffusion is hindered by the cooling rates reaching the mid-10^4 to mid-10^5 K/s ranges (Fig. 12).

Previous works demonstrated that the scanning pattern can significantly influence transformation behavior, with even slight thermal history variations potentially causing notable phase transformation changes. [60]. The effect leading to retained austenite here may be of mechanical nature, supporting the argument that metastable austenite is stabilized by residual stresses deep into the bulk, as suggested in [61,62]. These works demonstrate that mechanical factors such as stress state (in surface or in bulk) can independently control retained-austenite amount, distribution and stability.

The amounts of secondary crystalline phase as low as observed in this work call for methods of characterization with high sensitivity and spatial resolution, such as SEM EBSD imaging. EBSD mapping enabled visualization of individual precipitates seemingly formed at grain boundaries within the $\alpha|\alpha'$-Fe matrix, however, it did not allow to resolve mesoscale structures (Fig. 9). This is a consequence of the probing depth of the electron beam used in electron microscopy, too shallow to extract useful information from the bulk of the sample, as probing is limited to a depth of no more than 50 nm [63,64]. Moreover, austenite formed in 13Cr-4Ni martensitic steels can be stable at room temperature, but can undergo stress-induced transformation to martensite [65]. Therefore, stress introduced in the material during mechanical polishing may lead to austenite-to-martensite transformation in metastable austenitic–ferritic compositions [66]. In other words, mechanical sample preparation affects the results obtained from surface-sensitive techniques such as EBSD or lab-based XRD in reflection mode up to 10 μm below the surface of the sample, as described in [66,67], and thus is not representative of the bulk material. Given the limitations of surface-sensitive techniques described above, the integration of more diverse bulk-sensitive approaches such as 3DXRD or scanning 3DXRD could offer valuable insights to complete the 3D μXRD scanning imaging performed in this work. These techniques enable three-dimensional mapping of both crystallographic phase, orientations and internal strains at the grain and sub-grain scale, probing further into the interplay between the effects of thermal cycling, scanning strategy, and geometry on retained austenite formation and residual stress development [68–70]. Electrochemical polishing is a sample preparation technique that allows metals with metastable phases to be prepared in a stress-free conditions and in the first approach, this technique was used for samples presented in this work. [67]. Although it allowed to see a very few austenite grains, their amount, size and distribution did not permit to observe the structures identified in μXRD mapping. Eventually, ion milling with argon (Ar) was chosen as a way to get rid of the mechanically altered outer layer and as an attempt at reaching the sub-surface — or bulk-region. However, also in this case, the spatial concentration of FCC precipitates was not sufficient to observe the structures visible in μXRD imaging using EBSD. This is a strong argument for the high relevance of synchrotron XRD mapping in transmission mode when attempting to detect ordered crystalline macro-structures as presented in this work.

4.2. Effect of cooling rates on the formation of γ-phase

The presence of similar structures despite the lack of elemental segregation was also reported in [19], although the Fe-0.45C steel powder used in that work has a much higher C content and a simpler chemical composition with 0.18 wt% Si and 0.08 wt% Mn, thus leaving more weight to carbon segregation mechanisms. In that work, it was postulated that austenite forms within the solid material around the melt pool tracks. This occurs in the region of the material at the vicinity of the liquid (the Heat-Affected Zone, HAZ) that reaches temperatures above Ae1. If the material is quenched below the M_s temperature (start of the martensite transition), austenite phase will transform to martensite; however, if it is not quenched below the M_f temperature (*i.e.* the lower end of the martensite transformation temperature), a certain amount of austenite remains untransformed. Therefore, the cooling rates preceding the moment the material reaches M_f define the final amount of retained austenite. The influence of carbon content on martensite transformation temperatures in steels has been extensively studied in research: increasing carbon content decreases both the M_s and the M_f (associated to the bainite start temperature, B_s) in an exponential manner [71,72]. Moreover, the difference between M_s and M_f is also depending on carbon content, and in this work, given the carbon content capped at 0.03 wt%, this difference is expected to be $\Delta T \approx 100$ K [59].

During PBF, the material in the vicinity of the molten volume is heated above the austenite stability temperature. Depending on the cooling rates, determined by the laser processing parameters and the sample geometry, a portion of this material will contain a certain amount of retained austenite after reaching room temperature. If the low amount of C present in this 415 stainless steel (< 0.03 wt% C) contributes to the formation of γ-Fe through carbon segregation mechanisms, it is expected to happen at very small scales and in very small amounts [59]. The amount of retained austenite in the studied samples was indeed very low, and did not exceed 0.5 wt%. However, synchrotron XRD measurements did not detect the presence of any carbide/carbo-nitride phases that would be a sign of carbon nano-segregation, normally favoring the formation of austenite.

The XRF experiments presented in this work did not show any segregation of Mn/Ni atoms in a scale corresponding to the distribution of the FCC phase, which could be caused by incomplete diffusion during solidification and would lead to FCC phase stabilization, even in nominally low-alloying FM compositions like AISI 415 steel.

Operando XRD measurements performed for 2 types of samples allowed to observe the austenite phase formation and transition to martensite during cooling, as well as to directly link these processes to the cooling rates. Significant heat accumulation observed in bulk sample sB has resulted in a relatively slow cooling rate of $2*10^3$ K/s at M_s (Fig. 12), which in turn has led to a significant amount of austenite to remain present after cooling (Fig. 10). In the case of the measurement performed for the wall sample sW, the estimated cooling rates were significantly higher, reaching beyond 10^5 K/s after solidification, and above $2 \cdot 10^4$ K/s at the calculated M_s temperature. These significantly different cooling rates resulted in noticeably different solidification paths, first allowing for the formation of δ-ferrite phase, followed by the γ-phase, which completely transformed into the martensitic phase after about 90 ms.

The operando XRD studies have shown that the process of retained austenite formation is very sensitive to cooling rates in MetcoAdd 415 steel. Higher cooling rates decrease the probability of austenite retention, whereas slower cooling may lead to a significant amount of austenite phase. The cooling rates in the samples studied ex-situ (s0, s90, s15) by multimodal chemical imaging could not be measured. However, given the faster laser scanning speed, the lower energy density, and the larger size of samples s0, s90, and s15, a significantly lower heat accumulation and higher cooling rates are expected for these samples — as compared to sample sB measured operando in reflection mode. A similar dependence of the cooling rates on laser speed and power was demonstrated in literature for different materials [73–75]. On the other hand, heat accumulation in samples s0, s90, and s15 should be higher than for the wall samples measured operando in

transmission mode (sW), built from a single laser track. Additionally, the geometry of the wall samples results in higher cooling rates.

The top layer of these cuboid samples cools faster than inside the bulk, driven by radiation and atmospheric convection. The effect of sample geometry on cooling rates was discussed in [57]. This resulted in the lack (or very small amounts) of retained austenite observed in the top layers of ex-situ samples, just like in the case of operando wall samples (sW). However, in the HAZ, where cooling only occurs through heat conduction, slower cooling rates allow for austenite retention.

4.3. On the presence of δ-phase during solidification

The presence or absence of δ-phase during cooling is expected to be linked to the cooling rates [76,77]. The formation of δ-phase during cooling in the PBF process has been reported in transmission mode for 0.35C hot-work tool steel in [77] at cooling rates slower than 10^6 K/s, but not at faster cooling rates in reflection mode. In 0.79C M50 Tool Steel [76] however, it was not observed for cooling rates of 10^5 K/s, although it was predicted to form as the first phase after solidification in CALPHAD-based calculations. The authors of that work have postulated that the 10^5 K/s cooling rate suppressed the formation of the δ-phase. In this work, the δ-phase was observed for cooling rates around 10^5 K/s for the sW-type samples, but not in the case of the 10^4 K/s for the sB-type samples, which is in contradiction with the propositions made in [76,77] that cooling rates higher than 10^5 K/s lead to the absence of the δ-phase. These results show that cooling rates are not the only factor that determines the presence of the δ-phase in the solidification path. On the other hand, in both cited works [76,77] and the study presented here, the δ-phase was observed only in the case of measurements performed in transmission mode using samples with a "wall geometry". This indicates that δ-phase formation may be dependent also on the sample's and/or measurement geometry. Although the amount of δ-phase plays a major role in its detectability, the measurement geometry may be critical in the case of very low amounts, as the measurements in transmission mode probe a significantly larger volume, deeper below the surface, while the measurements in reflection mode only probe a shallow fraction of the material, *i.e.* less than $\approx$ 5-10 μm below the surface. Furthermore, it should be noted that the δ-phase was observed only in measurements performed during remelting of AM-built structures — without powder. It could therefore be affected by chemical changes that occurred in the already laser-processed material. Nevertheless, the question of the presence of δ-phase in the solidification path during PBF manufacturing of martensitic steels is beyond the scope of this work and shall be further studied to gain a complete understanding.

5. Conclusions

Synchrotron-based 2D and 3D μXRD mapping enabled the detection of localized austenitic regions within the ferritic–martensitic matrix, revealing variations in phase composition throughout the sample volume, despite the rapid cooling rates and solidification conditions, usually expected to favor ferritic–martensitic microstructures. In particular, 3D μXRD allowed for the reconstruction of the austenitic microstructures within the bulk of the manufactured FM steel. It revealed interconnected austenitic networks along build-directional columnar grains, a feature undetectable in 2D analyses. A clear correlation between the laser scanning strategy and the austenite distribution was found, while no link to chemical segregation at the corresponding scale of the main alloying elements was observed. The resulting diffraction patterns were analyzed to quantify the volume fraction of crystalline phases and to map their spatial distributions.

Operando XRD experiments monitored real-time phase transformations during the AM process, linking them to cooling rates in various sample geometries. These results are crucial for correlating process parameters with material outcomes and identifying strategies to prevent unwanted phases.

The multimodal characterization approach presented in this work stresses the importance of combining advanced analytical techniques to tackle the complexities of AM-specific micro-structures. This study reveals the formation, distribution, and properties of unexpected austenitic phase regions, aiding the optimization of AM-manufactured RAFM steels for nuclear fusion. It shows the critical interplay between process parameters, thermal history, and microstructural evolution, offering a pathway to enhance the performance and reliability of components in nuclear environments. These results build upon our understanding that the properties of complex AM components, which might contain wall-like and deep bulk features, vary significantly from one region to the other. Our results underscore the importance of post-manufacturing heat treatments for additive-manufactured RAFM steels, which can help in removing the RA from the microstructure. However, as demonstrated in the literature, retained austenite can have an impact on microstructure and the amount of reversed austenite in steels after post-manufacturing heat treatment. Therefore, the results presented here need to be considered in the process of recrystallization. Further investigations for nuclear applications requiring irradiation and both strength and fracture resistance are needed to address the strong thermomechanical constraints during the operation, as well as to assess the impact (positive or negative) of these specific phase structures on the material's radiation aging properties.

CRediT authorship contribution statement

Natan Garrivier: Writing – original draft, Visualization, Software, Resources, Project administration, Methodology, Investigation, Formal analysis, Data curation. **Steven Van Petegem:** Writing – review & editing, Software, Investigation, Funding acquisition, Data curation. **Manuel Pouchon:** Writing – review & editing, Funding acquisition. **Markus Strobl:** Writing – review & editing, Funding acquisition. **Enrico Tosoratti:** Writing – review & editing, Resources, Investigation. **Adam Cretton:** Writing – review & editing, Investigation. **Ken Vidar Falch:** Investigation, Data curation. **Dario Ferreira Sanchez:** Investigation, Formal analysis, Data curation. **Malgorzata Grazyna Makowska:** Writing – original draft, Visualization, Supervision, Software, Project administration, Investigation, Funding acquisition, Formal analysis, Data curation.

Declaration of competing interest

The authors declare that they have no known competing financial interests or personal relationships that could have appeared to influence the work reported in this paper.

Acknowledgments

The authors would like to thank particularly Dr. Karsten Kunze of ScopeM/ETH Zürich for his support & assistance in performing EBSD measurements; Eliot Jermann for performing the complementary SEM/EDX measurements; Dr. William Hearn, Dr. Steve Gaudez for their precious inputs in data interpretation and Dr. Jan Čapek for the preliminary EBSD analysis. We acknowledge DESY (Hamburg, Germany), a member of the Helmholtz Association HGF, for the provision of experimental facilities. Parts of this research were carried out at PETRA III, under the allocated beamtime proposal I-20240075 EC. Data was collected using the P06 beamline provided by DESY Photon Science. We would like to thank the P06 beamline staff for their assistance during the experiments. We also acknowledge PSI (Villigen, Switzerland), for funding this research and the provision of experimental facilities. Parts of this research were carried out at SLS, under the allocated proposal 20222009. Data was collected using the MicroXAS beamline provided by PSI Center for Photon Science. We would like to thank the MicroXAS

beamline staff for their assistance during the experiments. This work was funded by the Paul Scherrer Institute through the PSI Research Grant 2021.

Appendix A. Supplementary data

Supplementary material related to this article can be found online at https://doi.org/10.1016/j.addma.2025.105055.

Data availability

Data will be made available on request.

References

[1] L. Forest, L.V. Boccaccini, L. Cogneau, A.L. Puma, H. Neuberger, S. Pascal, J. Rey, N. Thomas, J. Tosi, M. Zmitko, Test blanket modules (ITER) and breeding blanket (DEMO): History of major fabrication technologies development of HCLL and HCPB and status, Fusion Eng. Des. 154 (2020) 111493, http://dx.doi.org/10.1016/j.fusengdes.2020.111493, https://linkinghub.elsevier.com/retrieve/pii/S0920379620300417.

[2] S. Bonk, H. Neuberger, D. Beckers, J. Koch, S. Antusch, M. Rieth, Additive manufacturing technologies for EUROFER97 components, J. Nucl. Mater. 548 (2021) 152859, http://dx.doi.org/10.1016/j.jnucmat.2021.152859, https://linkinghub.elsevier.com/retrieve/pii/S0022311521000829.

[3] T. Hirai, F. Escourbiac, S. Carpentier-Chouchana, A. Fedosov, L. Ferrand, T. Jokinen, V. Komarov, A. Kukushkin, M. Merola, R. Mitteau, R. Pitts, W. Shu, M. Sugihara, B. Riccardi, S. Suzuki, R. Villari, [Iter] tungsten divertor design development and qualification program, Fusion Eng. Des. 88 (9–10) (2013) 1798–1801, http://dx.doi.org/10.1016/j.fusengdes.2013.05.010, https://linkinghub.elsevier.com/retrieve/pii/S0920379613004420.

[4] T. Muroga, J.M. Chen, V.M. Chernov, R.J. Kurtz, M.L. Flem, Present status of vanadium alloys for fusion applications, J. Nucl. Mater. 455 (1) (2014) 263–268, http://dx.doi.org/10.1016/j.jnucmat.2014.06.025, https://www.sciencedirect.com/science/article/pii/S0022311514003821.

[5] T. Nagasaka, T. Muroga, 6.01 - Vanadium for Nuclear Systems, in: R. E. Stoller (Eds.) R. J. M. Konings (Ed.), Comprehensive Nuclear Materials (Second Edition), second ed., Elsevier, Oxford, 2020, pp. 1–18, http://dx.doi.org/10.1016/B978-0-12-803581-8.00730-X, https://www.sciencedirect.com/science/article/pii/B978012803581800730X.

[6] Y. Katoh, K. Ozawa, C. Shih, T. Nozawa, R.J. Shinavski, A. Hasegawa, L.L. Snead, Continuous SiC fiber, CVI SiC matrix composites for nuclear applications: Properties and irradiation effects, J. Nucl. Mater. 448 (1) (2014) 448–476, http://dx.doi.org/10.1016/j.jnucmat.2013.06.040, https://www.sciencedirect.com/science/article/pii/S0022311513008647.

[7] D.J.M. King, A.J. Knowles, D. Bowden, M.R. Wenman, S. Capp, M. Gorley, J. Shimwell, L. Packer, M.R. Gilbert, A. Harte, High temperature zirconium alloys for fusion energy, J. Nucl. Mater. 559 (2022) 153431, http://dx.doi.org/10.1016/j.jnucmat.2021.153431, https://www.sciencedirect.com/science/article/pii/S0022311521006516.

[8] S.J. Zinkle, Advanced materials for fusion technology, Fusion Eng. Des. 74 (1) (2005) 31–40, https://www.sciencedirect.com/science/article/pii/S0920379605004060.

[9] G. Pintsuk, G. Aiello, S.L. Dudarev, M. Gorley, J. Henry, M. Richou, M. Rieth, D. Terentyev, R. Vila, Materials for in-vessel components, Fusion Eng. Des. 174 (2022) 112994, http://dx.doi.org/10.1016/j.fusengdes.2005.08.008, https://linkinghub.elsevier.com/retrieve/pii/S0920379621007699.

[10] H. Tanigawa, E. Gaganidze, T. Hirose, M. Ando, S. Zinkle, R. Lindau, E. Diegele, Development of benchmark reduced activation ferritic/martensitic steels for fusion energy applications, Nucl. Fusion 57 (9) (2017) 092004, http://dx.doi.org/10.1088/1741-4326/57/9/092004, publisher: IOP Publishing.

[11] L. Boccaccini, F. Arbeiter, P. Arena, J. Aubert, L. Bühler, I. Cristescu, A.D. Nevo, M. Eboli, L. Forest, C. Harrington, F. Hernandez, R. Knitter, H. Neuberger, D. Rapisarda, P. Sardain, G. Spagnuolo, M. Utili, L. Vala, A. Venturini, P. Vladimirov, G. Zhou, Status of maturation of critical technologies and systems design: Breeding blanket, Fusion Eng. Des. 179 (2022) 113116, http://dx.doi.org/10.1016/j.fusengdes.2022.113116, https://linkinghub.elsevier.com/retrieve/pii/S0920379622001168.

[12] G. x. Qiu, H. z. Zhang, J. n. Li, Q. Li, Y. k. Yang, X. m. Li, [Effects of Heat] Treatment and Aging on Microstructural and Mechanical Properties of RAFM Steel, JOM 77 (4) (2025) 2109–2120, http://dx.doi.org/10.1007/s11837-024-07031-1, https://link.springer.com/10.1007/s11837-024-07031-1.

[13] W. Chen, H. Jia, H. Cao, J. Suh, S.H. Kang, J. Yu, Tailoring the microstructure and tensile properties of multi-component nano oxide-dispersion-strengthened RAFM steel fabricated by LPBF through heat treatment, Mater. Today Commun. 42 (2025) 111570, http://dx.doi.org/10.1016/j.mtcomm.2025.111570, https://www.sciencedirect.com/science/article/pii/S2352492825000820.

[14] Z. Xia, J. Xu, J. Shi, T. Shi, C. Sun, D. Qiu, Microstructure evolution and mechanical properties of reduced activation steel manufactured through laser directed energy deposition, Addit. Manuf. 33 (2020) 101114, http://dx.doi.org/10.1016/j.addma.2020.101114, https://linkinghub.elsevier.com/retrieve/pii/S2214860419318536.

[15] I.K. Robin, D.J. Sprouster, N. Sridharan, L.L. Snead, S.J. Zinkle, Synchrotron based investigation of anisotropy and microstructure of wire arc additive manufactured Grade 91 steel, J. Mater. Res. Technol. 29 (2024) 5010–5021, http://dx.doi.org/10.1016/j.jmrt.2024.02.230, https://www.sciencedirect.com/science/article/pii/S2238785424005246.

[16] T. Gräning, N. Sridharan, [Benchmarking a 9Cr]-2WVTa Reduced Activation Ferritic Martensitic Steel Fabricated via Additive Manufacturing, Metals 12 (2) (2022) http://dx.doi.org/10.3390/met12020342, https://www.mdpi.com/2075-4701/12/2/342.

[17] M.G. Jiang, Z.W. Chen, J.D. Tong, C.Y. Liu, G. Xu, H.B. Liao, P. Wang, X.Y. Wang, M. Xu, C.S. Lao, Strong and ductile reduced activation ferritic/martensitic steel additively manufactured by selective laser melting, Mater. Res. Lett. 7 (10) (2019) 426–432, http://dx.doi.org/10.1080/21663831.2019.1631224, https://www.tandfonline.com/doi/full/10.1080/21663831.2019.1631224.

[18] C.-Y. Chen, I. Chiang, Y.-C. Kang, The effect of retained austenite on austenite reversion behavior and corresponding mechanical properties of Ti–Mo precipitation hardening stainless steels, J. Mater. Res. Technol. 35 (2025) 1476–1493, http://dx.doi.org/10.1016/j.jmrt.2025.01.131, https://linkinghub.elsevier.com/retrieve/pii/S2238785425001322.

[19] W. Hearn, K. Lindgren, J. Persson, E. Hryha, In situ tempering of martensite during laser powder bed fusion of Fe-0.45 c steel, Materialia 23 (2022) 101459, publisher: Elsevier.

[20] T.J. Lienert, S.A. Maloy, B.P. Eftink, D. Vega, Additive manufacturing of ferritic/martensitic steel with improved high temperature strength, 2022.

[21] S. Gaudez, J. Macchi, G. Geandier, S. Denis, S.Y.P. Allain, Thermodynamic Approach to Describe the Martensite Phase Transformation Kinetics via the Stabilization of Austenite, Met. Mater. Trans. A 55 (3) (2024) 812–826, http://dx.doi.org/10.1007/s11661-023-07287-3, https://link.springer.com/10.1007/s11661-023-07287-3.

[22] K. Chadha, Y. Tian, P. Bocher, J.G. Spray, C. Aranas, [Microstructure Evolution], Mechanical Properties and Deformation Behavior of an Additively Manufactured Maraging Steel, Materials 13 (10) (2020) http://dx.doi.org/10.3390/ma13102380, https://www.mdpi.com/1996-1944/13/10/2380.

[23] T. Lyu, M.K. Keshavarz, S. Patel, M.J.R. Haché, C. Cheng, X. Shang, M. Vlasea, Y. Zou, Melting mode driven tuning of local microstructure and hardness in laser powder bed fusion of 18Ni-300 maraging steel, Materialia 35 (2024) 102113, http://dx.doi.org/10.1016/j.mtla.2024.102113, https://www.sciencedirect.com/science/article/pii/S2589152924001108.

[24] A. Królicka, J. Malawska, [Recent Progress] in Laser Powder Bed Fusions Processes of Advanced High-Strength Steels, Materials 17 (19) (2024) http://dx.doi.org/10.3390/ma17194699, https://www.mdpi.com/1996-1944/17/19/4699.

[25] F.F. Conde, J.D. Escobar, J.P. Oliveira, A.L. Jardini, W.W.B. Filho, J.A. Avila, Austenite reversion kinetics and stability during tempering of an additively manufactured maraging 300 steel, Addit. Manuf. 29 (2019) 100804, http://dx.doi.org/10.1016/j.addma.2019.100804, https://www.sciencedirect.com/science/article/pii/S2214860418308030.

[26] M.A. Zaccone, G. Krauss, Elastic Limit and Microplastic Response of Hardened Steels, Met. Trans. A 24 (10) (1993) 2263–2277, http://dx.doi.org/10.1007/BF02648600.

[27] M.H. Dao, J. Lou, Simulations of Laser Assisted Additive Manufacturing by Smoothed Particle Hydrodynamics, Comput. Methods Appl. Mech. Engrg. 373 (2021) 113491, http://dx.doi.org/10.1016/j.cma.2020.113491, https://linkinghub.elsevier.com/retrieve/pii/S0045782520306769.

[28] M. Markl, C. Körner, Multiscale Modeling of Powder Bed–Based Additive Manufacturing, Annu. Rev. Mater. Res. 46 (1) (2016) 93–123, http://dx.doi.org/10.1146/annurev-matsci-070115-032158, https://www.annualreviews.org/doi/10.1146/annurev-matsci-070115-032158.

[29] J.H.K. Tan, S.L. Sing, W.Y. Yeong, Microstructure modelling for metallic additive manufacturing: a review, Virtual Phys. Prototyp. 15 (1) (2020) 87–105, http://dx.doi.org/10.1080/17452759.2019.1677345, https://www.tandfonline.com/doi/full/10.1080/17452759.2019.1677345.

[30] B. Vrancken, R.K. Ganeriwala, M.J. Matthews, Analysis of laser-induced microcracking in tungsten under additive manufacturing conditions: Experiment and simulation, Acta Mater. 194 (2020) 464–472, http://dx.doi.org/10.1016/j.actamat.2020.04.060, https://linkinghub.elsevier.com/retrieve/pii/S1359645420303281.

[31] A. Razavykia, E. Brusa, C. Delprete, R. Yavari, [An Overview] of Additive Manufacturing Technologies—A Review to Technical Synthesis in Numerical Study of Selective Laser Melting, Materials 13 (17) (2020) 3895, http://dx.doi.org/10.3390/ma13173895, https://www.mdpi.com/1996-1944/13/17/3895.

[32] X. Song, S. Feih, W. Zhai, C.-N. Sun, F. Li, R. Maiti, J. Wei, Y. Yang, V. Oancea, L. Romano Brandt, A.M. Korsunsky, Advances in additive manufacturing process simulation: Residual stresses and distortion predictions in complex metallic components, Mater. Des. 193 (2020) 108779, http://dx.doi.org/10.1016/j.matdes.2020.108779, https://linkinghub.elsevier.com/retrieve/pii/S0264127520303130.

[33] S. Sumarli, E. Polatidis, F. Malamud, M. Busi, C. Navarre, R. Esmaeilzadeh, R. Logé, M. Strobl, Neutron Bragg edge imaging for strain characterization in powder bed additive manufacturing environments, J. Mater. Res. Technol. 21 (2022) 4428–4438, https://linkinghub.elsevier.com/retrieve/pii/S2238785422017537.

[34] S.G. Jeong, S.Y. Ahn, E.S. Kim, G.M. Karthik, Y. Baik, D. Seong, Y.S. Kim, W. Woo, H.S. Kim, Effect of substrate yield strength and grain size on the residual stress of direct energy deposition additive manufacturing measured by neutron diffraction, Mater. Sci. Eng.: A 851 (2022) 143632, http://dx.doi.org/10.1016/j.jmrt.2022.11.047, https://linkinghub.elsevier.com/retrieve/pii/S0921509322010164.

[35] M. Busi, E. Polatidis, F. Malamud, W. Kockelmann, M. Morgano, A. Kaestner, A. Tremsin, N. Kalentics, R. Logé, C. Leinenbach, T. Shinohara, M. Strobl, Bragg edge tomography characterization of additively manufactured 316L steel, Phys. Rev. Mater. 6 (5) (2022) 053602, http://dx.doi.org/10.1103/PhysRevMaterials.6.053602, https://link.aps.org/doi/10.1103/PhysRevMaterials.6.053602.

[36] S. Hocine, S. Van Petegem, U. Frommherz, G. Tinti, N. Casati, D. Grolimund, H. Van Swygenhoven, A miniaturized selective laser melting device for operando X-ray diffraction studies, Addit. Manuf. 34 (2020) 101194, http://dx.doi.org/10.1016/j.addma.2020.101194, https://linkinghub.elsevier.com/retrieve/pii/S2214860420305662.

[37] M. Makowska, F. Verga, S. Pfeiffer, F. Marone, C. Chang, C. Schlepütz, K. Florio, K. Wegener, T. Graule, S.V. Petegem, Operando tomographic microscopy during laser-based powder bed fusion, Prepr. Rev. (Jul. 2022) http://dx.doi.org/10.21203/rs.3.rs-1874885/v1, https://www.researchsquare.com/article/rs-1874885/v1.

[38] V. Pandiyan, G. Masinelli, N. Claire, T. Le-Quang, M. Hamidi-Nasab, C. d. Formanoir, R. Esmaeilzadeh, S. Goel, F. Marone, R. Logé, S.V. Petegem, K. Wasmer, Deep learning-based monitoring of laser powder bed fusion process on variable time-scales using heterogeneous sensing and operando X-ray radiography guidance, Addit. Manuf. 58 (2022) 103007, http://dx.doi.org/10.1016/j.addma.2022.103007, https://www.sciencedirect.com/science/article/pii/S2214860422004006.

[39] C.L.A. Leung, S. Marussi, R.C. Atwood, M. Towrie, P.J. Withers, P.D. Lee, In situ X-ray imaging of defect and molten pool dynamics in laser additive manufacturing, Nat. Commun. 9 (1) (2018) 1355, http://dx.doi.org/10.1038/s41467-018-03734-7.

[40] L. Wang, Y. Zhang, H.Y. Chia, W. Yan, Mechanism of keyhole pore formation in metal additive manufacturing, Npj Comput. Mater. 8 (1) (2022) 22, http://dx.doi.org/10.1038/s41524-022-00699-6.

[41] S. Hocine, H. Van Swygenhoven, S. Van Petegem, Verification of selective laser melting heat source models with operando X-ray diffraction data, Addit. Manuf. 37 (2021) 101747, http://dx.doi.org/10.1016/j.addma.2020.101747, https://linkinghub.elsevier.com/retrieve/pii/S2214860420311192.

[42] A. Muther, M.G. Makowska, Z.L. Zhang, F. Verga, F. Marone, N. Garrivier, A. Cretton, S.V. Petegem, M. Bambach, M. Afrasiabi, Identifying melt pool behavior in ceramics PBF-LB via operando synchrotron tomographic microscopy and high-fidelity process modeling, Addit. Manuf. 103 (2025) 104756, http://dx.doi.org/10.1016/j.addma.2025.104756, https://www.sciencedirect.com/science/article/pii/S2214860425001204.

[43] C. Ioannidou, H.-H. König, N. Semjatov, U. Ackelid, P. Staron, C. Koerner, P. Hedström, G. Lindwall, In-situ synchrotron X-ray analysis of metal Additive Manufacturing: Current state, opportunities and challenges, Mater. Des. 219 (2022) 110790, publisher: Elsevier.

[44] N. An, S. Shuai, T. Hu, C. Chen, J. Wang, Z. Ren, Application of synchrotron X-ray imaging and diffraction in additive manufacturing: a review, Acta Met. Sin. (English Letters) (2022) 1–24, Publisher: Springer.

[45] K.K. Singh, A. Wakai, A. Moridi, Advancements in operando X-ray techniques for metal additive manufacturing, Commun. Mater. 5 (1) (2024) 258, http://dx.doi.org/10.1038/s43246-024-00699-7.

[46] A.W. Colldeweih, M.G. Makowska, O. Tabai, D.F. Sanchez, J. Bertsch, [Zirconium hydride] Phase Mapping in Zircaloy-2 Cladding Containing Delayed Hydride Cracking, SSRN Electron. Journal (2022) http://dx.doi.org/10.2139/SSRN.4245032, Publisher: Elsevier BV. https://papers.ssrn.com/abstract=4245032.

[47] M. Makowska, P.V.W. Sasikumar, L. Hagelüken, D.F. Sanchez, N. Casati, F. Marone, G. Blugan, J. Brugger, H. Van Swygenhoven, Cracks, porosity and microstructure of Ti modified polymer-derived SiOC revealed by absorption-, XRD- and XRF-contrast 2D and 3D imaging, Acta Mater. 198 (2020) 134–144, http://dx.doi.org/10.1016/j.actamat.2020.07.067, publisher: Pergamon. https://linkinghub.elsevier.com/retrieve/pii/S135964542030584X.

[48] C.G. Anchieta, B.A. Francisco, J.P. Júlio, P. Trtik, A. Bonnin, G. Doubek, D.F. Sanchez, LiOH Decomposition by NiO/ZrO2 in Li-Air Battery: Chemical Imaging with Operando Synchrotron Diffraction and Correlative Neutron/X-Ray Computed-Tomography Analysis, Small Methods 8 (10) (2024) 2301749, http://dx.doi.org/10.1002/SMTD.202301749, publisher: John Wiley & Sons, Ltd. https://onlinelibrary.wiley.com/doi/full/10.1002/smtd.202301749. https://onlinelibrary.wiley.com/doi/abs/10.1002/smtd.202301749. https://onlinelibrary.wiley.com/doi/10.1002/smtd.202301749.

[49] H. Ding, C. Gausse, M.C. Wilkins, L.M. Mottram, M.C. Stennett, D. Grolimund, R. Tappero, S. Nicholas, S. Sun, T. Shiba, C. Paraskevoulakos, N.C. Hyatt, C.L. Corkhill, Chemical characterisation of degraded nuclear fuel analogues simulating the Fukushima Daiichi nuclear accident, Npj Mater. Degrad. 2022 6:1 6 (1) (2022) 1–13, http://dx.doi.org/10.1038/s41529-022-00219-3, publisher: Nature Publishing Group. https://www.nature.com/articles/s41529-022-00219-3.

[50] L. Mansur, A. Rowcliffe, R. Nanstad, S. Zinkle, W. Corwin, R. Stoller, Materials needs for fusion, Generation IV fission reactors and spallation neutron sources – similarities and differences, J. Nucl. Mater. 329–333 (2004) 166–172, http://dx.doi.org/10.1016/j.jnucmat.2004.04.016, https://linkinghub.elsevier.com/retrieve/pii/S0022311504001473.

[51] V.A. Solé, E. Papillon, M. Cotte, P. Walter, J. Susini, A multiplatform code for the analysis of energy-dispersive X-ray fluorescence spectra, Spectrochim. Acta Part B: At. Spectrosc. 62 (1) (2007) 63–68, http://dx.doi.org/10.1016/j.sab.2006.12.002, https://www.sciencedirect.com/science/article/pii/S0584854706003764.

[52] J. Kieffer, G. Ashiotis, [Pyfai]: a Python library for high performance azimuthal integration on GPU, 2014, _eprint: 1412.6367. https://arxiv.org/abs/1412.6367.

[53] W. v. Aarle, W.J. Palenstijn, J.D. Beenhouwer, T. Altantzis, S. Bals, K.J. Batenburg, J. Sijbers, The ASTRA Toolbox: A platform for advanced algorithm development in electron tomography, Ultramicroscopy 157 (2015) 35–47, http://dx.doi.org/10.1016/j.ultramic.2015.05.002, https://www.sciencedirect.com/science/article/pii/S0304399115001060.

[54] W. v. Aarle, W.J. Palenstijn, J. Cant, E. Janssens, F. Bleichrodt, A. Dabravolski, J.D. Beenhouwer, K.J. Batenburg, J. Sijbers, Fast and flexible X-ray tomography using the ASTRA toolbox, Opt. Express 24 (22) (2016) 25129–25147, http://dx.doi.org/10.1364/OE.24.025129, https://opg.optica.org/oe/abstract.cfm?URI=oe-24-22-25129.

[55] S. Hocine, H. Van Swygenhoven, S. Van Petegem, C.S.T. Chang, T. Maimaitiyili, G. Tinti, D. Ferreira Sanchez, D. Grolimund, N. Casati, Operando X-ray diffraction during laser 3D printing, Mater. Today 34 (2020) 30–40, http://dx.doi.org/10.1016/j.mattod.2019.10.001, https://linkinghub.elsevier.com/retrieve/pii/S136970211930803X.

[56] I. Johnson, A. Bergamaschi, H. Billich, S. Cartier, R. Dinapoli, D. Greiffenberg, M. Guizar-Sicairos, B. Henrich, J. Jungmann, D. Mezza, A. Mozzanica, B. Schmitt, X. Shi, G. Tinti, Eiger: a single-photon counting x-ray detector, J. Instrum. 9 (05) (2014) C05032, http://dx.doi.org/10.1088/1748-0221/9/05/C05032.

[57] M. Chen, M. Simonelli, S. Van Petegem, Y. Yau Tse, C. Sin Ting Chang, M. Grazyna Makowska, D. Ferreira Sanchez, H. Moens-Van Swygenhoven, A quantitative study of thermal cycling along the build direction of Ti-6Al-4V produced by laser powder bed fusion, Mater. Des. 225 (2023) 111458, http://dx.doi.org/10.1016/j.matdes.2022.111458, https://linkinghub.elsevier.com/retrieve/pii/S0264127522010814.

[58] J. Ingber, M. Kunert, Prediction of the Martensite Start Temperature in High-Carbon Steels, Steel Res. Int. 93 (5) (2022) http://dx.doi.org/10.1002/srin.202100576, https://onlinelibrary.wiley.com/doi/10.1002/srin.202100576. publisher: Wiley.

[59] J.D. Verhoeven, Steel metallurgy for the non-metallurgist, ASM Int. (2007).

[60] C. Zhang, H. Ozcan, L. Xue, K.C. Atli, R. Arróyave, I. Karaman, A.H. Elwany, On the effect of scan strategies on the transformation behavior and mechanical properties of additively manufactured NiTi shape memory alloys, J. Manuf. Process. (2022) https://api.semanticscholar.org/CorpusID:252960937.

[61] M. Hayama, Y. Maki, S. Kikuchi, J. Komotori, Change Behavior of Retained Austenite and Residual Stress on Carburized SCM420H Steel during Fatigue Process, ISIJ Int. 64 (3) (2024) 597–604, http://dx.doi.org/10.2355/isijinternational.ISIJINT-2023-421, https://www.jstage.jst.go.jp/article/isijinternational/64/3/64_ISIJINT-2023-421/_article.

[62] B. AlMangour, J.-M. Yang, Understanding the deformation behavior of 17-4 precipitate hardenable stainless steel produced by direct metal laser sintering using micropillar compression and TEM, Int. J. Adv. Manuf. Technol. 90 (1–4) (2017) 119–126, http://dx.doi.org/10.1007/s00170-016-9367-9, http://link.springer.com/10.1007/s00170-016-9367-9.

[63] S.F. Bordín, S. Limandri, J.M. Ranalli, G. Castellano, [EBSD] spatial resolution for detecting sigma phase in steels, Ultramicroscopy 171 (2016) 177–185, http://dx.doi.org/10.1016/j.ultramic.2016.09.010, https://www.sciencedirect.com/science/article/pii/S0304399116301991.

[64] W. Wisniewski, S. Saager, A. Böbenroth, C. Rüssel, Experimental evidence concerning the significant information depth of electron backscatter diffraction (EBSD), Ultramicroscopy 173 (2017) 1–9, http://dx.doi.org/10.1016/j.ultramic.2016.11.004, https://www.sciencedirect.com/science/article/pii/S0304399116303163.

[65] D. Thibault, P. Bocher, M. Thomas, J. Lanteigne, P. Hovington, P. Robichaud, Reformed austenite transformation during fatigue crack propagation of 13%Cr–4%Ni stainless steel, Mater. Sci. Eng.: A 528 (21) (2011) 6519–6526, http://dx.doi.org/10.1016/j.msea.2011.04.089, https://www.sciencedirect.com/science/article/pii/S0921509311005351.

[66] L.A. Pinto, D. Pérez Escobar, O.S. Santos, N.I. Lopes, J.R. Carneiro, R. Ribeiro-Andrade, Influence of surface preparation method on retained austenite quantification, Mater. Today Commun. 24 (2020) 101226, http://dx.doi.org/10.1016/J.MTCOMM.2020.101226, publisher: Elsevier..

[67] T. Juuti, S. Uusikallio, A. Kaijalainen, E. Heinonen, N.T. Tun, D.A. Porter, The Effect of Sample Preparation on the Microstructure of Austenitic-Ferritic Stainless Steel, in: THERMEC 2016 879of Materials Science Forum, Trans Tech Publications Ltd, 2017, pp. 873–878, http://dx.doi.org/10.4028/www.scientific.net/MSF.879.873.

[68] J.A.D. Ball, C. Davis, C. Slater, H. Vashishtha, M. Said, L. Hébrard, F. Steinhilber, J.P. Wright, T. Connolley, S. Michalik, D.M. Collins, Grain-level effects on in-situ deformation-induced phase transformations in a complex-phase steel using 3DXRD and EBSD, Acta Mater. 265 (2024) 119608, http://dx.doi.org/10.1016/j.actamat.2023.119608, https://www.sciencedirect.com/science/article/pii/S1359645423009369.

[69] J.A.D. Ball, A. Kareer, O.V. Magdysyuk, S. Michalik, T. Connolley, D.M. Collins, Revealing per-grain and neighbourhood stress interactions of a deforming ferritic steel via three-dimensional X-ray diffraction, Commun. Mater. 5 (1) (2024) 27, http://dx.doi.org/10.1038/s43246-024-00466-8.

[70] Y. Zhang, J. Ball, A. Henningsson, J. Wright, L. Lopez, D. Jobes, H. Proudhon, J.V. Gordon, Unveiling 3D sub-grain residual stresses in as-built additively manufactured steel using scanning 3DXRD, Mater. Res. Lett. 13 (7) (2025) 700–708, http://dx.doi.org/10.1080/21663831.2025.2502502, publisher: Taylor & Francis _eprint:.

[71] H. Kawata, K. Fujiwara, M. Takahashi, Effect of Carbon Content on Bainite Transformation Start Temperature in Low Carbon Fe–9Ni–c Alloys, ISIJ Int. 57 (10) (2017) 1866–1873, http://dx.doi.org/10.2355/isijinternational.ISIJINT-2017-239.

[72] S.M.C. v. Bohemen, Bainite and martensite start temperature calculated with exponential carbon dependence, Mater. Sci. Technol. 28 (4) (2012) 487–495, http://dx.doi.org/10.1179/1743284711Y.0000000097, _eprint: DOI: 10.1179/1743284711Y.0000000097.

[73] P. Scheel, P. Markovic, S.V. Petegem, M.G. Makowska, R. Wrobel, T. Mayer, C. Leinenbach, E. Mazza, E. Hosseini, A close look at temperature profiles during laser powder bed fusion using operando X-ray diffraction and finite element simulations, Addit. Manuf. Lett. 6 (2023) 100150, http://dx.doi.org/10.1016/j.addlet.2023.100150, https://www.sciencedirect.com/science/article/pii/S2772369023000312.

[74] K. Kosiba, T. Gustmann, J.T. Kim, J. Seok, J. Jung, L. Beyer, S. Scudino, L. Giebeler, J. Han, J.K. Hufenbach, Experimental cooling rates during high-power laser powder bed fusion at varying processing conditions, J. Alloys Compd. 967 (2023) 171773, http://dx.doi.org/10.1016/j.jallcom.2023.171773, https://www.sciencedirect.com/science/article/pii/S0925838823030761.

[75] S. Pauly, P. Wang, U. Kühn, K. Kosiba, Experimental determination of cooling rates in selectively laser-melted eutectic Al-33Cu, Addit. Manuf. 22 (2018) 753–757, http://dx.doi.org/10.1016/j.addma.2018.05.034, https://www.sciencedirect.com/science/article/pii/S2214860418300733.

[76] H. Zhang, A. Özsoy, G. Soundarapandiyan, M.G. Makowska, P. Diaz-del Castillo, S. Van Petegem, B. Chen, Stepwise Martensite Phase Transformation in M50 Tool Steel During Laser Powder Bed Fusion Via Operando X-Ray Diffraction. Steven and Chen, Bo, Stepwise Martensite Phase Transformation in M50 Tool Steel During Laser Powder Bed Fusion Via Operando X-ray Diffraction.

[77] H.-H. König, N.H. Pettersson, A. Durga, S.V. Petegem, D. Grolimund, A.C. Chuang, Q. Guo, L. Chen, C. Oikonomou, F. Zhang, G. Lindwall, Solidification modes during additive manufacturing of steel revealed by high-speed X-ray diffraction, Acta Mater. 246 (2023) 118713, http://dx.doi.org/10.1016/j.actamat.2023.118713, https://www.sciencedirect.com/science/article/pii/S1359645423000459.